第 16 回
核燃焼プラズマ
統合コード研究会

16th Burning Plasma Simulation Initiative (BPSI) Meeting

日時：2018 年 11 月 29 日(木)－30 日(金)
場所：九州大学筑紫キャンパス
応用力学研究所 2 階大会議室

第 16 回核燃焼プラズマ統合コード研究会

16th Burning Plasma Simulation Initiative (BPSI) Meeting

(Ver.1.1)

日時：2018 年 11 月 29 日(木)－30 日(金)
場所：九州大学筑紫キャンパス　応用力学研究所 2 階大会議室

(18 min talk+7 min discuss or (15 or 10) min talk+5 min discuss)

11 月 29 日(木)

9:10 – 12:30　核融合エネルギーフォーラムサブクラスターとの合同会合

12:30 – 13:30　昼休み

13:30 – 13:40　はじめに　　村上（京大）
(座長：村上)
13:40 – 14:05　講演 1-1　　林（量研）
Predictive integrated modelling of plasmas and their operation scenarios towards exploitation of JT-60SA experiment
14:05 – 14:30　講演 1-2　　矢本（量研）
Extension of SONIC code toward mixed-impurity seeding capability
14:30 – 14:55　講演 1-3　　本多（量研）
Development of the integrated model with the iterative solver GOTRESS
14:55 – 15:20　講演 1-4　　福山（京大）
Progress in kinetic full wave analyses in fusion plasmas

15:20 – 15:40　休憩

(座長：林)
15:40 – 16:05　講演 1-5　　登田（核融合研）
Modeling of turbulent particle and heat transport in helical plasmas based on gyrokinetic analysis
16:05 – 16:30　講演 1-6　　成田（量研）
Particle transport modeling based on gyrokinetic analyses of JT-60U plasmas
16:30 – 16:55　講演 1-7　　村上（京大）
Simulation study of toroidal flow generation by ECH in non-axisymmetric tokamak plasmas
16:55 – 17:15　講演 1-8　　山本（京大）
Effects of electron cyclotron heating on the toroidal flow in HSX plasmas
17:15　散会

18:30 – 21:00　懇親会（炙り炉端 山尾 博多駅前にて）

11 月 30 日(金)

9:30 – 9:35 事務連絡
(座長：糟谷)
9:35 – 10:00 講演 2-1 Yagi 矢木（量研）
Revisit ion-mixing mode
10:00 – 10:25 講演 2-2 Kosuga 小菅（九大）
How pattern is selected in drift wave turbulence: role of parallel flow shear (tentative)
10:25 – 10:45 講演 2-3 Gyung Jin Choi (Seoul Univ.)
Gyrokinetic simulation study of parity dependence of magnetic transport

10:45 – 11:05 休憩

(座長：登田)
11:05 – 11:30 講演 2-4 大澤（九大）
Stable structure of hydrogen in tungsten di-vacancy and its isotope effect
11:30 – 11:55 講演 2-5 沼波（核融合研）
Kinetic simulations for particle transport of multi-species plasmas in LHD
11:55 – 12:20 講演 2-6 奴賀（核融合研）
Analysis of energetic particle confinement in LHD using neutron measurement and Fokker-Planck codes

12:20 – 13:30 昼休み

(座長：矢木)
13:30 – 13:50 講演 3-1 前田（京大）
Modelling of heat transport in LHD using neural network with non-dimensional input parameters
13:50 – 14:05 講演 3-2 凌（京大）
Integrated simulation study of LHD type fusion reactor by TASK3D
14:05 – 14:20 講演 3-3 森下（京大）
Integrated transport simulation of LHD plasma using data assimilation
14:20 – 14:45 講演 3-4 佐々木（九大）
Chirality of helical flows in plasma turbulence
14:45 – 15:10 講演 3-5 糟谷（九大）
Study of plasma instability by numerical simulations in basic experimental devices
15:10 – 15:30 まとめ 糟谷（九大）
15:30 散会

JT-60SA実験に向けたプラズマと運転シナリオの統合予測モデリング

Predictive integrated modelling of plasmas and their operation scenarios towards exploitation of JT-60SA experiment

林　伸彦 [1)]、ガルシア ジェロニモ [2)]、JT-60SAチーム
N. Hayashi [1)], J. Garcia [2)], and the JT-60SA Team

1) 量研、2) フランス原子力庁 磁場閉じ込め核融合研究所
1) QST, 2) CEA IRFM

Modelling strategy towards exploitation of JT-60SA experiment

JT-60SA is a large superconducting tokamak and will start plasma operations in 2020 well in advance of ITER operation. The JT-60SA mission is to contribute to early realization of fusion energy by supporting the exploitation of ITER and by complementing ITER in resolving key issues for DEMO reactors. For the mission, JT-60SA is equipped with flexibly applicable actuators, i.e., negative- and positive-ion-based neutral beams (NBs) and electron cyclotron waves, to control heating, current and torque profiles (total input power P_{in}=41 MW). With the actuators, JT-60SA explores inductive, advanced inductive and steady-state high-beta plasma operation scenarios [1]. Integrated modelling and prediction of plasmas and their operation scenarios plays a key role to plan experiments and prepare the model validation through the prediction confirmation in real experiments. For the purpose, not only JT-60SA modelling itself but also the validation of models for JT-60U and JET experiments to develop the best modelling framework to predict, and the model verification between integrated codes to improve the prediction reliability have been carried out in the close collaboration between Japan and EU [1,2]. These modelling activities are carried out intensely towards the start of JT-60SA experiments and the following results were obtained.

Prediction results

The integrated code TOPICS with the CDBM anomalous heat transport model validated by JT-60U/JET experiments [2] is used for the plasma prediction of high-beta steady-state scenario, which is the most challenging scenario due to simultaneous achievement of full current drive, low divertor heat load and so on, with their strong interactions. The previous prediction [2] used a simple NB model without a finite-orbit effect of fast ions, however, the prediction depends on the accuracy of NB models in the verification between integrated codes. The prediction is improved using the Orbit-Following Monte-Carlo code OFMC, which is also verified by the ASCOT code. Pedestal profiles are determined on the basis of EPED1 model. Temperature profiles are solved, while the electron density profile is prescribed. By the power control with P_{in}~26 MW, a steady-state plasma (β_N=4.3, H_H=1.6) is obtained with an internal transport barrier (ITB) as shown in Fig.1(a). Even with small power perturbations (+/− 0.2 MW) to the above reference case, ITB continuously moves outward/inward, β_N increases/decreases (Fig.1(b)) and the current becomes over/inductively driven. Although the plasma is unstable against the perturbations, the long time scale of deviations is about the current diffusion time in the ITB region (order of 10 s in Fig.1(b)) and enables to sustain the ITB position and target performance by enhancing/reducing powers every several to ten seconds without their runaways.

Other integrated modelling for inductive scenarios reveals that the rotation with the neoclassical toroidal viscosity (NTV) due to the toroidal magnetic field ripple degrades the pedestal height, but it is high enough to achieve target parameters, and error field correction coils in JT-60SA have the potential to control the rotation by changing NTV. The obtained predictions clarify the JT-60SA capability to explore the plasma scenarios indispensable to ITER and DEMO.

[1] G. Giruzzi et al., Nucl. Fusion **57**(2017)085001

[2] N. Hayashi et al., Nucl. Fusion **57**(2017)126037

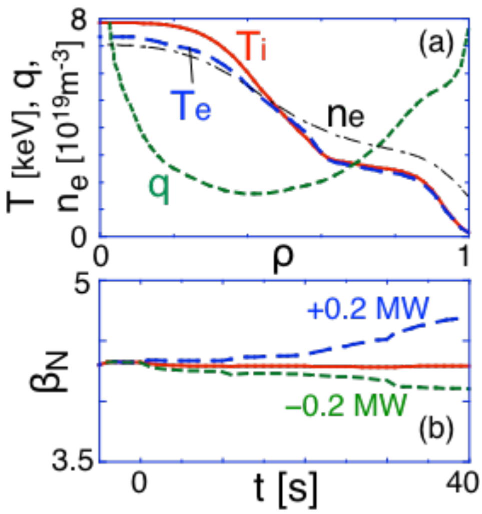

Fig.1 (a) Profiles of ion/electron temperatures, safety factor and prescribed electron density in a JT-60SA steady-state plasma with β_N=4.3. (b) Time evolution of β_N in a reference case (solid line, profiles are shown in (a), input power is adjusted at t=0 s and kept constant to 40 s) and two cases with ±0.2 MW perturbations from t=0 s.

Extension of SONIC code toward mixed-impurity seeding capability

Shohei YAMOTO[1)], Kazuo HOSHINO[2)], Tomohide NAKANO[1)], Nobuhiko HAYASHI[1)]

[1)]QST, [2)]Keio Univ.

1. Introduction

The JT-60SA tokamak is now being constructed and is expected to ignite the first plasma at 2020 and to perform ITER-supporting and -complementing experiments from 2023 under various operation scenarios. One of the underlying operation scenarios is the high-beta operation under full non-inductive current drive conditions (steady-state high-beta operation) [1]. The operation will take place with impurity seeding to reduce the heat load towards the divertors and with keeping the separatrix density low enough to match the core operation condition. On the other hand, the concentration of the impurities in the core causes a harmful effect to sustain the high-performance plasma by radiation cooling and dilution. Therefore, it is important to establish a method to control the impurity transport in the core and SOL/divertor regions. So far, a favourable spatial distribution of radiation power has been achieved by Ne + Ar (mixed gas) seeding experiment in JT-60U, i.e. the radiated power is almost localized in the divertor region and as a consequence, better energy confinement than Ne-only and Ar-only cases has been achieved [2]. However, the interpretative and predictive simulation of such mixed gas seeding operation has not been performed. This is partly because the number of impurity species that the previous version of integrated divertor plasma transport code SONIC [3,4] could kinetically solve was limited to one. The issue has been essentially resolved by restructuring SONIC code with Multiple-Program Multiple-Data (MPMD) framework [5], which allows SONIC to calculate transport processes of two impurity species by a kinetic impurity transport code IMPMC. The extended SONIC code was applied to the analysis of the JT-60SA divertor plasma with two impurity species, i.e., the intrinsic C and seeded Ar gas impurities, and demonstrated the radiative divertor plasma scenario [5]. The purpose of this paper is to examine the effects of different impurity seeding species in the JT-60SA divertor plasmas step-by-step in order to study the potential impurity seeding operation regime. Aiming for this purpose, the SONIC code has been further extended to handle three or more impurity species kinetically based on the MPMD framework mentioned above. Now the SONIC code is capable of calculating the mixed seeding impurities Ne + Ar and intrinsic C transport by IMPMC. The impurity-impurity interaction such as the physical sputtering of C by Ne and Ar bombardment has been also implemented. The effects of seeding mixture of Ne and Ar in JT-60SA steady-state high-beta operation scenario is demonstrated by means of the extended version of SONIC.

2. Calculation condition

Figure 1 shows the computational grid for JT-60SA. The locations of the injection ports of each impurity species are also shown in Fig. 1. The intrinsic C impurities are also considered in the calculation.

The following steps are set to discuss the effects of additional Ne seeding taking the Ar seeding case [5] as a reference; (i) the parametric survey of the Ne seeding rate (0.01 – 0.1 Pa m^3/s) with other parameters kept the same as ref. [5], and (ii) the exploration of the D_2 gas puff and the seeding rate of impurities which satisfies the target parameters of the scenario (the electron density at the separatrix $n_{e,sep}$~1.7×10^{19} m^{-3}, and the divertor heat load q_{div}<10 MW/m^2). The Ar seeding rate is automatically adjusted to keep the total radiation power to be 13MW in the plasma.

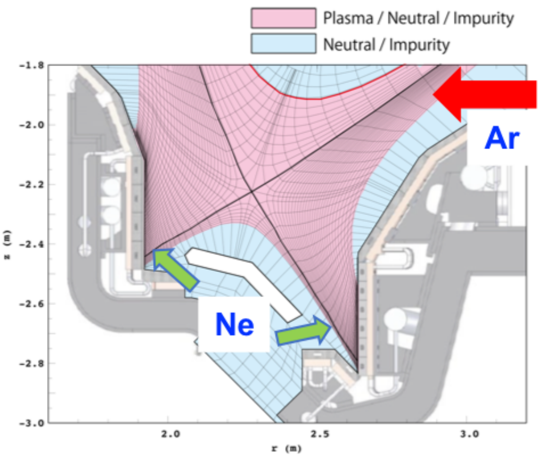

Fig. 1 Computational grid for JT-60SA. The locations of the injection ports of each impurity species are also indicated.

3. Results

3.1 Step (i)

Figure 2 shows the fractional radiation power in the divertor region as a function of Ne seeding rate. As shown in Fig. 2, the radiation power is more localized in the divertor region as the Ne seeding rate increases. This is due to the additional seeding of Ne impurities, which are mostly radiate in the divertor region. Furthermore, the Ar radiation power in the divertor region is also increased because the lower charge state densities of Ar has been increased in the Ne+Ar seeding case.

In addition, the electron and D^+ densities at the outer midplane are reduced compared to the Ar seeding case as shown in Fig. 3. The possible reason is that the radiation power localized in the divertor region leads to the cooler electron temperature in the divertor region. In that case, the recycling is enhanced and the neutral pressure becomes high. Therefore, the pumping flux becomes high and the D^+ density is decreased. Therefore, the Ne+Ar seeding is effective to obtain radiative divertor operation with keeping the upstream electron density lower than the Ar-only seeding case. However, the mechanism is not fully understood and thus we will investigate in detail in near future.

3.2 Step (ii)

In order to obtain the Ne+Ar seeding operation conditions which satisfies the target parameters of the scenario, D_2 gas seeding rate has been increased with fixed seeding rate of Ne 0.1 Pa m^3/s. A set of parameters (Ar seeding: 0.1 Pa m^3/s, Ne seeding: 0.1 Pa m^3/s, and D_2 seeding: 10.0 Pa m^3/s) has been found, which satisfies the target parameters. The radial distribution of the electron density at the outer midplane becomes ~1.7×10^{19} m^{-3}, and the target heat load along the outer divertor plate becomes less than 10 MW/m^2 as seen from Fig. 4. The spatial

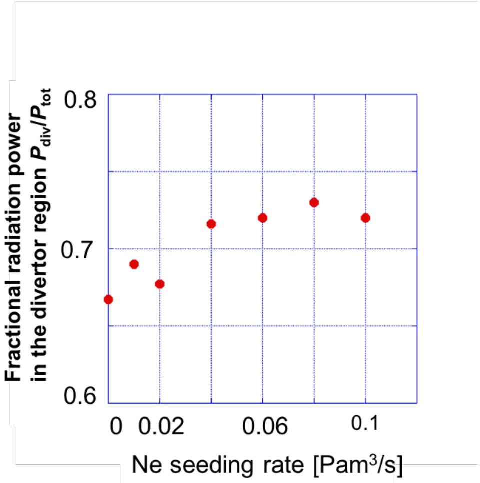

Fig. 2 Fractional radiation power in the divertor region as a function of Ne seeding rate.

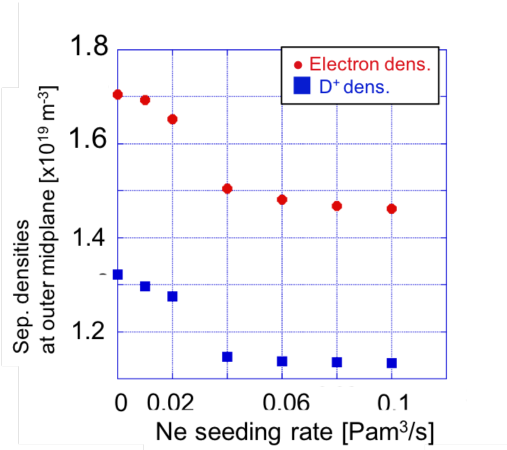

Fig. 3 Electron and D^+ separatrix densities at outer midplane as a function of Ne seeding rate.

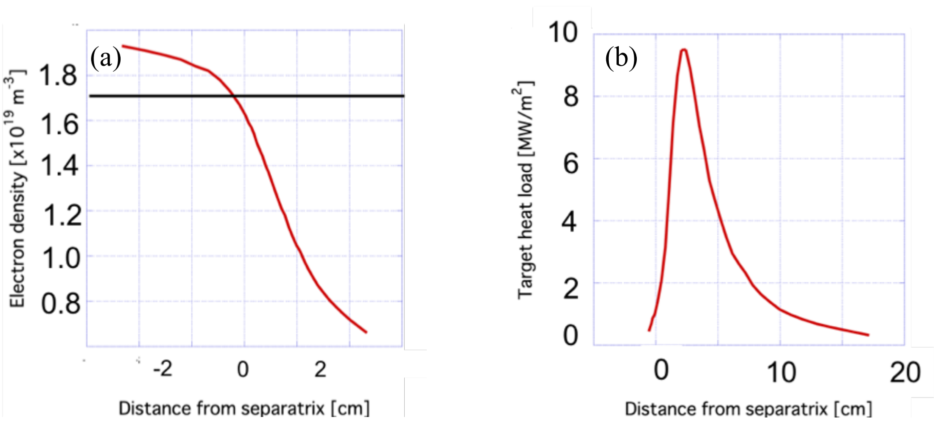

Fig. 4 Radial distributions of the plasma parameters; (a) the electron density at the outer midplane, and (b) the target heat load along the outer divertor plate

distributions of the radiation power density for each impurity species are shown in Fig. 5. We have also compared the obtained result with Ne-only and Ar-only seeding cases with respect to the core dilution and core radiation. In Ne+Ar case, the fuel purity at the edge ($n_{\mathrm{D}^+}/n_{\mathrm{e}}$) become highest among Ar-only, Ne-only, and Ar+Ne cases ($n_{\mathrm{D}^+}/n_{\mathrm{e}}\sim$ 0.79, 0.77, and 0.83 in each case, respectively), which is good for the core performance improvement. In addition, the Ar radiation power in the edge is reduced from 1.1MW (Ar-only case) to 0.6 MW (Ne+Ar case). Therefore, the Ar radiation in the core is possibly reduced in Ne+Ar case.

4. Summary

The purpose of this paper is to examine the effects of different impurity seeding species in the JT-60SA divertor plasmas step-by-step in order to study the potential impurity seeding operation regime. Aiming for this purpose, the SONIC code has been further extended to handle three or more impurity species kinetically based on the MPMD framework. Now the SONIC code is capable of calculating the mixed seeding impurities Ne + Ar and intrinsic C transport by IMPMC. The effects of seeding mixture of Ne and Ar in JT-60SA steady-state high-beta operation scenario is demonstrated by means of the extended version of SONIC. The following steps are set to discuss the effects of additional Ne seeding taking the Ar seeding case [5] as a reference; (i) the parametric survey of the Ne seeding rate (0.01 – 0.1 Pa m^3/s) with other parameters kept the same as ref. [5], and (ii) the exploration of the D_2 gas puff and the seeding rate of impurities which satisfies the target parameters of the scenario. In step (i), the radiation more localized in the divertor region can be seen as the Ne seeding rate increases. In addition, the electron and D^+ densities at the outer midplane are reduced compared to the Ar seeding case. The Ne+Ar seeding is effective to obtain radiative divertor operation with keeping the upstream electron density lower than the Ar-only seeding case. In step(ii), a set of parameters which satisfies the target parameters of the scenario have been achieved (Ar seeding rate: 0.1 Pa m^3/s, Ne seeding rate: 0.1 Pa m^3/s, and D_2 puff rate: 10.0 Pa m^3/s). In Ne+Ar case, the fuel purity at the edge ($n_{\mathrm{D}^+}/n_{\mathrm{e}}$) become highest among Ar-only, Ne-only, and Ar+Ne cases ($n_{\mathrm{D}^+}/n_{\mathrm{e}}\sim$ 0.79, 0.77, and 0.83 in each case, respectively), which is good for the core performance improvement. In addition, the Ar radiation power in the edge is reduced from 1.1MW (Ar-only case) to 0.6 MW (Ne+Ar case). Therefore, the Ar radiation in the core is possibly reduced in Ne+Ar case.

References

[1] JT-60SA Research Plan (http://www.jt60sa.org/pdfs/JT-60SA_Res_Plan.pdf)
[2] N. Asakura, *et al.*, Nucl. Fusion **49** (2009) 115010.
[3] H. Kawashima, *et al.*, Plasma Fusion Res. **1** (2006) 031.
[4] K. Shimizu, *et al.*, Nucl. Fusion **49** (2009) 065028.
[5] K. Hoshino, *et al.*, Contrib. Plasma Phys. **56** (2018) 638.

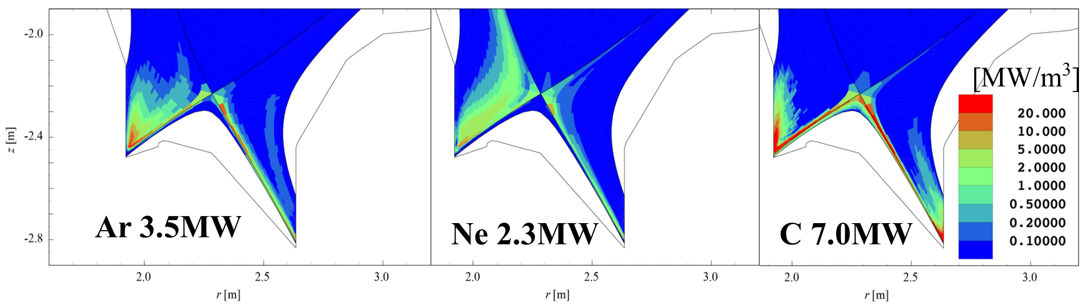

Fig. 4 The spatial distributions of radiation power density for each impurity species. The total radiation power of each impurity species is also indicated.

Development of the integrated model with the iterative solver GOTRESS

M. Honda, E. Narita and N. Hayashi

National Institutes for Quantum and Radiological Science and Technology, Naka, Ibaraki 311-0193 Japan

Introduction

The steady-state transport equation solver, GOTRESS, has been developed, which directly finds the solution where a transport flux matches an integral of sources and sinks using global optimization techniques such as a genetic algorithm and Nelder-Mead method [1]. So far, GOTRESS has been used in a manner that an equilibrium and source profiles are given in advance. For the purpose that GOTRESS is used to examine the feasibility of prescribed kinetic profiles used in an operation scenario and to develop a new scenario, however, a consistent solution among predicted kinetic profiles, an equilibrium and source and sink profiles must be necessary. This fact motivates us to develop a novel integrated model with GOTRESS as a kernel of the model.

GOTRESS

In the light of the aim of the code, GOTRESS is very similar to TGYRO [2]. Both codes solve a steady-state transport equation and calculate the kinetic profiles that give rise to the transport flux coinciding with the integral of source and sink profiles. However, they take a completely different approach to get a solution. While TGYRO discretizes the volume-integral form of the equation and solves it with Newton method and fixed point iteration, GOTRESS prepares the two kinds of the volume-integral equations and directly tries to find a solution of each equation, such as temperature and its radial derivative, using global optimization techniques. In doing so, GOTRESS can avoid possible oscillations originating from the discretization of the equation and the estimation of derivatives when a stiff transport model applies. Further details of the methodology can be consulted in [1].

GOTRESS+

TGYRO is characterized as a profile solver in the OMFIT framework [3], which is a comprehensive integrated modeling framework that has been developed to enable physics codes to interact in complicated workflows. As explained above, GOTRESS can naturally play a same role as TGYRO in an integrated modeling framework. Accordingly, the integrated model GOTRESS+ has been developed, mainly consisting of the equilibrium and current profile solver ACCOME [4] and the neutral beam (NB) heating code OFMC [5], other than GOTRESS. The settings of auxiliary heating systems such as NB heating and electron cyclotron heating (ECH) and the coils that support an equilibrium are described in an input file of ACCOME. The prescribed density and temperature profiles are also given as initial guess. After the iterative calculations in ACCOME, a consistent solution is obtained between an equilibrium and a current profile according to the given kinetic profiles. ACCOME also estimates ECH and EC current drive (ECCD). The profiles required for OFMC are sent to OFMC, and then the NB heating profiles and NB current drive (NBCD) are estimated. Now the current density profiles, the equilibrium and heating profiles have been computed, which are all required for GOTRESS. GOTRESS predicts the temperature profiles based on them. At this point, the first

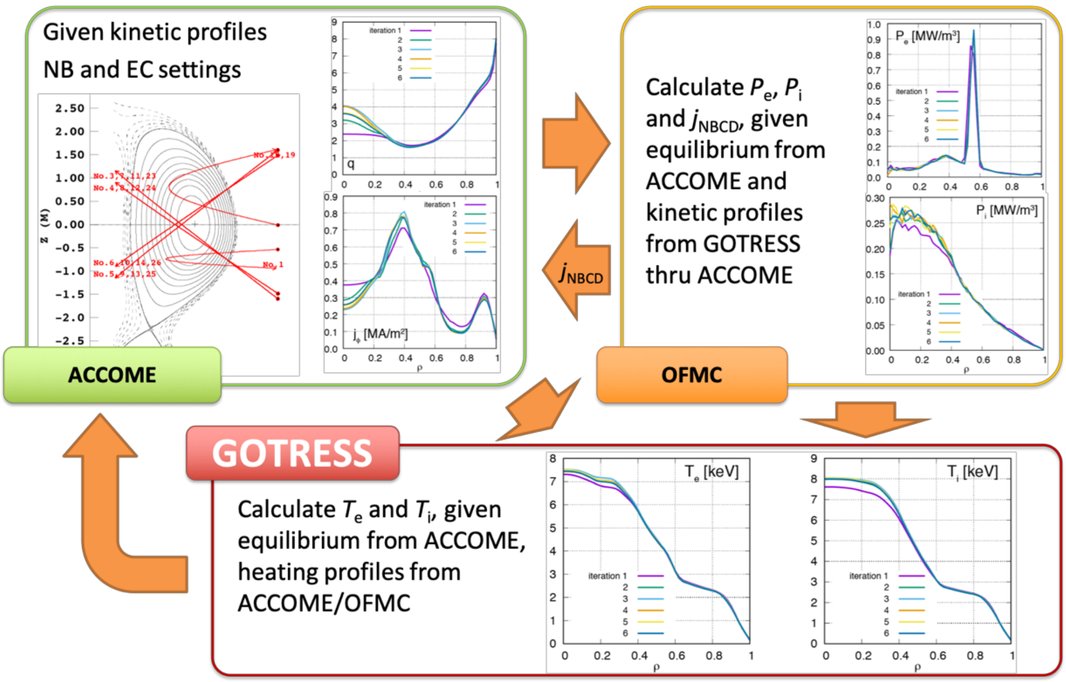

Fig. 1: Workflow of GOTRESS+. The predicted profiles are illustrated and each color of a line corresponds to the number of times of iteration.

iteration of GOTRESS+ is completed, as shown in Fig. 1. The predicted temperature profiles are sent to ACCOME and replaces the prescribed ones used in the first iteration. The second iteration then commences. Note that optionally ACCOME can make use of the NBCD profile calculated by OFMC instead of its own Fokker-Planck solver, but the choice is up to a user. This iteration continues until the profiles are well converged.

Comparison of the predicted profiles with TOPICS

TOPICS has already carried out the feasibility test of the high-β_N scenario in JT-60SA, so-called #5-1: B_T/I_p=1.72T/2.3MA, P_{NBI}/P_{ECH}=18.85MW/7MW [6]. GOTRESS+ now applies to this case. As shown in Fig. 2(a), both results are very good agreement in terms of ion temperature, even though they come from thoroughly different integrated models. Good agreement holds for electron temperature as well. When it comes to the residual ion power δP_i, which is the difference between the transport flux and the integral of sources and sinks, δP_i of GOTRESS+ is much smaller than that of TOPICS, indicating that the profiles predicted by GOTRESS+ approach to a steady state more closely. Time consumption of GOTRESS+ is 6,812 sec, which is much faster than that of TOPICS being 42,909 sec.

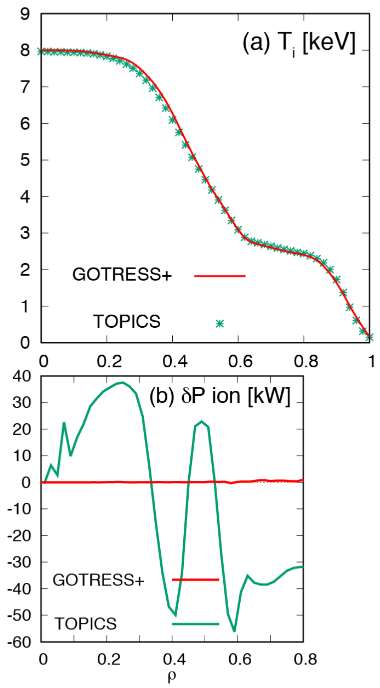

Fig. 2: Comparison of (a) T_i and (b)the residual ion power between GOTRESS+ and TOPICS.

References

[1] M. Honda, Comput. Phys. Commun. **231** (2018) 94.

[2] J. Candy et al., Phys. Plasmas **16** (2009) 060704.

[3] O. Meneghini et al., Nucl. Fusion **55** (2015) 083008.

[4] K. Tani, M. Azumi and R. S. Devoto, J. Comput. Phys. **98** (1992) 332.

[5] K. Tani, M. Azumi, H. Kishimoto and S. Tamura, J. Phys. Soc. Jpn. **50** (1981) 1726.

[6] N. Hayashi et al., *Proc. Int. Conf. on Fusion Energy (Ahmadabad, India, 2018)*, PPC/1-1 (2018).

Modeling of turbulent particle and heat transport in helical plasmas based on gyrokinetic analysis

S. Toda, M. Nakata, M. Nunami, A. Ishizawa[1], T. -H. Watanabe[2] and H. Sugama
National Institute for Fusion Science, Oroshi-cho 322-6, Toki, Gifu, 509-5292, Japan
[1]*Graduate School of Energy Science, Kyoto Uni., Gokasho, Uji, Kyoto, 611-0011, Japan*
[2]*Department of Physics, Nagoya University, Furo-cho, Nagoya, Aichi, 464-8602, Japan*

A quantitative prediction of turbulent transport is one of the most critical issues for realizing magnetic fusion energy. Recently, a large number of gyrokinetic simulations of the turbulent transport in toroidal plasmas have been performed. The gyrokinetic analysis results in tokamak and helical plasmas have been compared with the experimental observation results. The gyrokinetic simulation for helical plasmas consumes much larger computer resources than those for tokamak plasmas, because the former requires a large number of mesh points along field lines in order to resolve helical ripple structures. Since it is still not easy to couple the nonlinear gyrokinetic simulation with an integrated transport simulation code, especially for helical plasmas, the predictive model, which can quickly reproduce the nonlinear simulation results, is highly demanded. The GKV code [1] has been widely used to investigate the ion temperature gradient (ITG) mode and zonal flows in the Large Helical Device (LHD) for studying the turbulent transport. Gyrokinetic simulations using the adiabatic electron assumption are performed for the high and the low ion temperature LHD cases in shot number 88343 [2]. The reduced model for the ion heat diffusivity was proposed [3] to reproduce the nonlinear simulation results given by the turbulence simulation with adiabatic electrons. This reduced model is the function of the linear growth rate for the ITG mode and the zonal flow decay time. The ion energy flux by this reduced model is in good agreement with the experimental results for the high-T_i plasmas at $t = 2.2$s [3]. How to apply the reduced model of the turbulent ion heat diffusivity in the adiabatic electron condition to the transport code has been shown for helical plasmas [4]. The simulation in the kinetic electron condition shows the larger ion energy flux than the experimental results for the high-T_i plasmas [5]. On the other hand, the electron and ion energy fluxes obtained from the simulation with kinetic electrons are close to those of the experimental results in the low-T_i plasmas [5] at $t = 1.8$s. The simulation result with adiabatic electrons in the low-T_i plasmas shows that the ITG mode becomes stable around $\rho(= r/a) = 0.5$. This work [6] presents the predictive transport model for the particle and electron heat diffusivities in addition to the ion heat diffusivity, including the effect of kinetic electrons on the plasma instability. For the purpose, the gyrokinetic equations for both electrons and ions are solved to evaluate the diffusivities and fluxes of the heat and particle transport. When the small number for the wavelength was taken, the reduced model for the ion heat diffusivity was proposed [7]. The larger number of the wavelength in the wider wavelength region is taken than the previous simulation [7], to show the models for the particle and electron heat transport. The electron and ion heat diffusivity models are presented, to reproduce the nonlinear simulation results in terms of the linear growth rates and the linear response of zonal flows. The quasilinear flux models are presented to reproduce the particle transport in addition to the heat transport obtained by the gyrokinetic simulations.

The turbulence driven by the microinstabilities in LHD plasmas is studied, using the gyrokinetic local flux tube code GKV [1]. The electromagnetic gyrokinetic equations are solved for both electrons and ions. The temperature and density profiles, and field configuration obtained from the LHD experimental results of the high-T_i plasmas at $t = 2.2$s and of the low-T_i plasmas at

$t = 1.8$s and 1.9s [2] are used. The major radii of the LHD plasmas are given by $R = 3.75$m for the high-T_i plasmas and $R = 3.6$m for the low-T_i plasmas. In the low-T_i plasmas, the magnetic field configuration is shifted more inward than in the high-T_i plasmas. The generation of zonal flows can be enhanced in the inward shifted configuration [8]. The electron and ion heat diffusivities are represented in terms of the linear simulation results, $\mathcal{L}$ and $\tilde{\tau}_{ZF}$ as

$$\frac{\chi_e^{model}}{\chi_i^{GB}} = \frac{A_{1e}\mathcal{L}^{B_{1e}}}{A_{2e} + \tilde{\tau}_{ZF}^{B_{2e}}/\mathcal{L}^{B_{3e}}}, \tag{1}$$

and

$$\frac{\chi_i^{model}}{\chi_i^{GB}} = \frac{A_{1i}\mathcal{L}^{B_{1i}}}{A_{2i} + \tilde{\tau}_{ZF}^{B_{2i}}/\mathcal{L}^{B_{3i}}}, \tag{2}$$

where the coefficients are given by $A_{1e} = C_{1e}C_T^{\alpha_e+1-c\xi/b}C_z^{-\xi/b} = 1.3\times 10$, $A_{2e} = C_{2e}C_T^{1-c\xi/b}C_z^{-\xi/b} = 2.0$, $A_{1i} = C_{1i}C_T^{\alpha_i+1-c/(2b)}C_z^{-1/(2b)} = 2.6\times 10^2$ and $A_{2i} = C_{2i}C_T^{1-c/(2b)}C_z^{-1/(2b)} = 1.8\times 10$. The exponents are given by $B_{1e} = \alpha_e a = 0.30$, $B_{2e} = \xi/b = 0.62$, $B_{3e} = a(1-c\xi/b) = 0.63$, $B_{1i} = \alpha_i a = 0.66$, $B_{2i} = 1/(2b) = 3.1$ and $B_{3i} = a(1-c/(2b)) = 0.26$. Here, the variables are shown as $\alpha_e = 0.19$, $C_{1e} = 6.8\times 10^{-2}$, $C_{2e} = 2.1\times 10^{-2}$, $\xi = 0.10$, $\alpha_i = 0.41$, $C_{1i} = 0.13$, $C_{2i} = 4.9\times 10^{-2}$, $C_T = 6.6\times 10$, $a = 1.6$, $C_z = 0.19$, $b = 0.16$ and $c = 0.27$. The quantity $\mathcal{L}$ related with the mixing length estimate is defined as $\mathcal{L} \equiv \int(\tilde{\gamma}_{\tilde{k}_y}/\tilde{k}_y^2)d\tilde{k}_y$. The zonal flow decay time is defined by $\tau_{ZF} \equiv \int_0^{\tau_f} dt\mathcal{R}_{\tilde{k}_x}(t)$, where $\mathcal{R}_{\tilde{k}_x}(t) \equiv \left\langle \tilde{\phi}_{\tilde{k}_x,\tilde{k}_y=0}(t)\right\rangle / \left\langle \tilde{\phi}_{\tilde{k}_x,\tilde{k}_y=0}(t=0)\right\rangle$, the upper limit τ_f in the integral is set to $\tau_f = 30R/v_{ti}$ and $\tilde{\tau}_{ZF} = \tau_{ZF}/(R/v_{ti})$. The normalized electron and ion heat diffusivities $\bar{\chi}_e/\chi_i^{GB}$ and $\bar{\chi}_i/\chi_i^{GB}$ obtained from the nonlinear simulation are compared with the model predictions $\chi_e^{model}/\chi_i^{GB}$ and $\chi_i^{model}/\chi_i^{GB}$. The heat diffusivity models reproduce the nonlinear simulation results $\bar{\chi}_e/\chi_i^{GB}$ within the relative error 0.21 and $\bar{\chi}_i/\chi_i^{GB}$ within the relative error 0.20.

The quasilinear models are constructed for both the particle and the energy fluxes. In the quasi-linear flux formulation, the particle and energy fluxes are written as

$$\tilde{\Gamma}^{QL} = C_\Gamma \int \frac{\tilde{\Gamma}_{\tilde{k}_y}^{lin}}{\left\langle |\tilde{\phi}_{\tilde{k}_y}^{lin}|^2 \right\rangle} \left\langle |\tilde{\phi}_{\tilde{k}_y}^{NL}|^2 \right\rangle d\tilde{k}_y \tag{3}$$

and

$$\tilde{Q}_j^{QL} = C_{Q_j} \int \frac{\tilde{Q}_{j,\tilde{k}_y}^{lin}}{\left\langle |\tilde{\phi}_{\tilde{k}_y}^{lin}|^2 \right\rangle} \left\langle |\tilde{\phi}_{\tilde{k}_y}^{NL}|^2 \right\rangle d\tilde{k}_y \tag{4}$$

for the species j, where the quantities with the superscripts lin and NL represent the linear and nonlinear simulation results. Here, the tilde $\tilde{}$ represents the normalization of the energy and particle fluxes by the values of $nT_i v_{ti}\rho_i^2/R^2$ and $nv_{ti}\rho_i^2/R^2$, respectively. The saturated intensity of the electrostatic potential fluctuation obtained from the nonlinear simulation, $\left\langle |\tilde{\phi}_{\tilde{k}_y}^{NL}|^2 \right\rangle$, is well fitted with the model function of $\tilde{\gamma}_{\tilde{k}_y}/\tilde{k}_y^2$ and the zonal flow decay time $\tilde{\tau}_{ZF}$,

$$\left\langle |\tilde{\phi}_{\tilde{k}_y}|^2 \right\rangle^{model} = \frac{C_{q1}(\tilde{\gamma}_{\tilde{k}_y}/\tilde{k}_y^2)^{\alpha_{q1}}}{C_{q2} + \tilde{\tau}_{ZF}^{\alpha_{ZF}}/(\tilde{\gamma}_{\tilde{k}_y}/\tilde{k}_y^2)^{\alpha_{q2}}} \tag{5}$$

at each $\tilde{k}_y$, where the parameters are $C_{q1} = 1.0\times 10^2$, $C_{q2} = 9.2\times 10^{-4}$, $\alpha_{q1} = 0.54$, $\alpha_{q2} = 0.12$ and $\alpha_{ZF} = 1.6$. To give the quasilinear flux models $\tilde{\Gamma}_{ql}^{model}$ and $\tilde{Q}_{j,ql}^{model}$ for the species j, the model function (5) is substituted into $\left\langle |\tilde{\phi}^{NL}_{\tilde{k}_y}|^2 \right\rangle$ in Eqs. (3) and (4). When the relative errors of the fluxes at each $\tilde{k}_y$ and the total fluxes integrated over the $\tilde{k}_y$ space are minimized between the nonlinear simulation results and the quasilinear flux models, the fitting parameters are determined as $C_{Q_e} = 0.78$, $C_{Q_i} = 0.58$ and $C_\Gamma = 0.73$. The fluxes from the nonlinear simulation $\tilde{\Gamma}^{NL}$, $\tilde{Q}_e^{NL}$ and $\tilde{Q}_i^{NL}$ are compared with the quasilinear flux models $\tilde{\Gamma}^{model}_{ql}$, $\tilde{Q}^{model}_{e,ql}$ and $\tilde{Q}^{model}_{i,ql}$, where the relative errors are given by 2.3, 0.24 and 0.24, respectively. The relative error shown above for the particle flux model is larger than those for the energy fluxes, because the quasilinear particle flux becomes close to zero at some radial points.

The gyrokinetic equations for both electrons and ions are solved by numerical simulations to model the diffusivities and the fluxes for the particle and heat transport. First, the electron and ion heat diffusivities are evaluated from the nonlinear simulations for high-T_i and low-T_i plasmas in the LHD, where the ITG mode is destabilized. The use of the linear simulation results enables us to reproduce the nonlinear simulation results for the electron and ion turbulent diffusivities by the heat diffusivity models shown. Since the density gradient is close to zero in some radial regions of the LHD plasmas, the reliable diffusivity model for the particle transport can not be shown. The quasilinear flux models for the electron and ion energy transport are proposed to reproduce the nonlinear simulation results. The nonlinear simulation results of the electron and ion energy fluxes are reproduced by the quasilinear flux models at the accuracy similar to that of the heat diffusivity models. In addition, the quasilinear particle flux model, which can be applicable even for the flattened density profiles in the LHD, is presented. Thus, the promising transport models, such as the heat diffusivity models and the quasilinear flux models for helical plasmas, are proposed based on the gyrokinetic simulation results. How to apply the ion heat diffusivity model to the dynamical transport code was already reported [4] and the dynamical transport simulation result for the ion temperature profile will be compared with the experimental result in the LHD. The study on how to install the electron heat diffusivity model and the quasilinear flux models to the dynamical transport code is in progress and will be reported elsewhere.
This work is partly supported by the NIFS Collaboration Research Programs, NIFS18KNST129, NIFS18KNXN363 (Plasma Simulator), NIFS18KNTT045, the JSPS KAKENHI Grant Number, 16K06941 and the Collaborative Research Program of Research Institute for Applied Mechanics, Kyushu University, 30FP-4. This work is carried out using the JFRS-1 supercomputer system at Computational Simulation Centre of International Fusion Energy Research Centre (IFERC-CSC) in Rokkasho Fusion Institute of QST (Project code: MTFHP).

[1] T. -H. Watanabe and H. Sugama, Nucl. Fusion **46**, 24 (2006).
[2] K. Tanaka et al., Plasma Fusion Res. **5**, S2053 (2010).
[3] M. Nunami, T. -H. Watanabe and H. Sugama, Phys. Plasmas **20**, 092307 (2013).
[4] S. Toda et al., J. Phys.: Conf. Ser. **561**, 012020 (2014).
[5] A. Ishizawa et al., Nucl. Fusion **57**, 066010 (2017).
[6] S. Toda et al., Phys. Plasmas accepted (2019).
[7] S. Toda et al., Plasma and Fusion Research **12**, 1303035 (2017).
[8] T. -H. Watanabe, H. Sugama and S. Ferrando-Margalet, Phys. Rev. Lett. **100**, 195002 (2008).

Particle transport modeling based on gyrokinetic analyses of JT-60U plasmas

E. Narita[1], M. Honda[1], M. Nakata[2,3], M. Yoshida[1], N. Hayashi[1], H. Takenaga[1]

[1]National Institutes for Quantum and Radiological Science and Technology, Naka, Ibaraki 311-0193, Japan

[2]National Institute for Fusion Science, Toki, Gifu 509-5292, Japan

[3]The Graduate University for Advanced Studies, Toki, Gifu 509-5292, Japan

1 Introduction

Fusion power strongly depends on the density and its profile, which are governed by turbulent particle transport in tokamak plasmas. Peaked density profiles are favorable for an increase in fusion power, and they tend to be observed in a low collisionality region [1, 2]. In addition to collisionality, particle sources due to external fueling such as the neutral-beam (NB) injection have been found to provide a contribution to density peaking [3, 4], but previous gyrokinetic studies on particle transport have shown a relationship between density peaking and dominant instabilities without finite particle sources [5]. Another issue on particle transport modeling is the computational cost required to predict the density profiles. When one uses the turbulent transport models based on the first-principles to calculate the turbulent particle flux, it takes from several hours to days to obtain a stationary-state density profile. In order to tackle the issue, a neural-network (NN) based approach has recently been undertaken, and NN-based transport models are now proposed [6, 7]. This paper presents a new one, which enables us to not only predict density profiles fast but also investigate effects of the turbulent transport mechanisms, considering the realistic particle sources.

2 Semi-empirical modeling of the quasilinear particle flux

The turbulent particle flux $\bar{\Gamma}$ for species a in a quasilinear limit is given as $\bar{\Gamma}_a = \bar{D}(R/L_{n_a} + C_{\mathrm{T}} R/L_{T_a} + C_{\mathrm{P}})$, where $\bar{D}$, R/L_{n_a} and R/L_{T_a} are the particle diffusivity in proportion to the fluctuation amplitudes, the density and temperature gradients, respectively, and all of them are non-dimensional. The diagonal diffusive term is proportional to R/L_{n_a}, and the off-diagonal component consists of the thermodiffusive term ($C_{\mathrm{T}} R/L_{T_a}$) and another pinch one (C_{P}). Applying a semi-empirical method [8], we have calculated C_{T}, C_{P} and $\bar{D}$, in the electron particle flux for a dataset of JT-60U H-mode plasmas [2], which are dominated by the ion temperature gradient (ITG) mode or the trapped electron mode (TEM). First, C_{T} and C_{P} are obtained by the linear calculations performed with the local flux-tube gyrokinetic code GKW [9, 10]. Next, assuming that the particle source from the NB injection $\bar{\Gamma}_{\mathrm{e,NB}}$ is balanced with the neoclassical particle flux $\bar{\Gamma}_{\mathrm{e,neo}}$ and the turbulent one $\bar{\Gamma}_{\mathrm{e,turb}}$: $\bar{\Gamma}_{\mathrm{e,NB}} + \bar{\Gamma}_{\mathrm{e,neo}} + \bar{\Gamma}_{\mathrm{e,turb}} = 0$, we evaluate $\bar{\Gamma}_{\mathrm{e,turb}}$ referred to as $\bar{\Gamma}_{\mathrm{e,exp}}$, and estimate $\bar{D}$ to match $\bar{\Gamma}_{\mathrm{e,exp}}$. In this way, C_{T}, C_{P} and $\bar{D}$ are obtained and they give the magnitude of the particle diffusion and pinch terms quantitatively.

3 Analyses of particle diffusion and pinch effects

The JT-60U experimental dataset referred to in the previous section has a variety of density peakedness. We have selected two plasmas from the dataset. The difference in the profile of the density gradient between the two cases is shown in figure 1(a). Hereafter, the peaked case and the other one are referred to as cases A and B, respectively. They have a comparable $\bar{\Gamma}_{\mathrm{e,exp}}$ in the core region due to the approximately equal external particle source from the NB injection. For the two cases, the diffusion and pinch terms are calculated using C_{T}, C_{P} and $\bar{D}$ obtained in section 2. As shown in figure 1(b), case A has the diffusion larger than case B especially around $\rho = 0.5$ due to the steeper density gradient. Since the sum of the diffusion and pinch terms is balanced with $\bar{\Gamma}_{\mathrm{e,exp}}$, it is found that the total pinch term of case A works to offset the large diffusion as shown in figure 1(c). Therefore, for case A, the inward pinch allows the peaked density profile that drives the large diffusion around $\rho = 0.5$. Both thermodiffusive and another pinch terms of case A contribute to a reduction in the particle flux in comparison with those of case B. The thermodiffusive term of case A is larger in the inward flux direction than that of case B due to the steeper electron temperature gradient for case A. On the other hand, the another-pinch terms of both cases are positive, corresponding the outward direction, and that of case A is closer to zero around $\rho = 0.5$. It has been found that C_{P} is almost proportional to the ion temperature gradient. Therefore, the difference in the another-pinch term between cases A and B is mainly due to the ion temperature gradient. These effects of the electron and ion temperature gradients on the pinch terms show that the ITG mode for case A is more suppressed than that for case B, and case A has a more TEM-like instability, resulting in the steeper density gradient for case A. The tendency agrees with the previous study [5], which shows that the transition from the ITG mode to the TEM in the ITG-dominated region accompanies the increase in the density gradient.

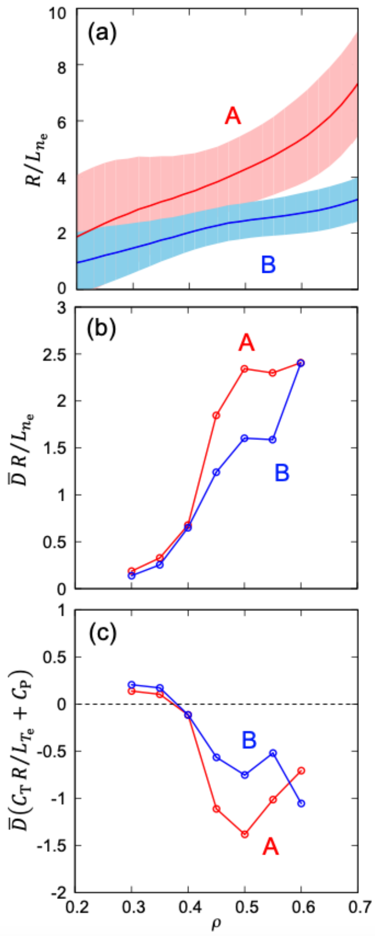

Figure 1. Radial profiles of (a) the density gradients with uncertainty bands, (b) the diffusion and (c) total pinch terms of cases A and B.

4 Development of a neural network particle transport model

In order to incorporate the understanding of the diffusion and pinch mechanisms into prediction of density profiles, C_{T}, C_{P} and $\bar{D}$ obtained in section 2 are used to train NNs. The constructed NN predicts C_{T}, C_{P} and $\bar{D}$ with 11 plasma parameters including R/L_n, $R/L_{T_{\mathrm{e}}}$ and $R/L_{T_{\mathrm{i}}}$, in ~ 0.02 seconds with a single CPU, and it has been validated using a subset that is not used for NN training, as shown in figure 2. Hereafter, the NN is used as the semi-empirical particle transport model to predict density profiles.

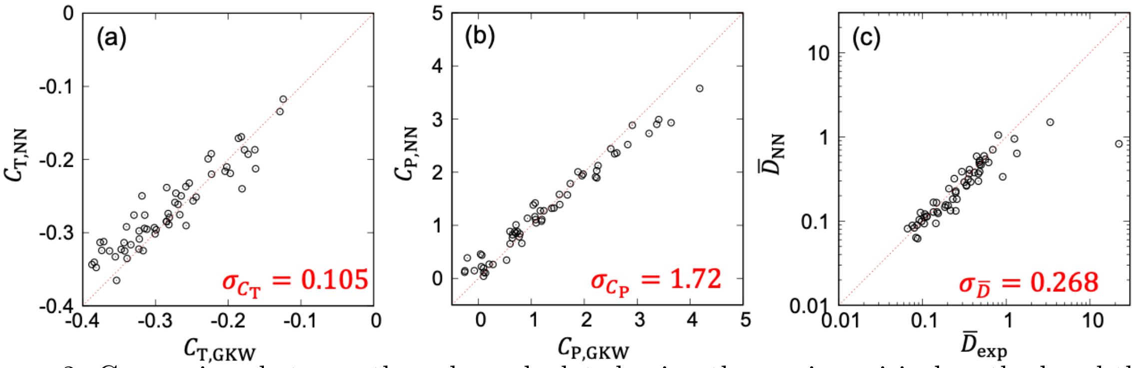

Figure 2. Comparison between the value calculated using the semi-empirical method and the NN regression for (a) C_{T}, (b) C_{P} and (c) $\bar{D}$. Here, σ is the root mean square error.

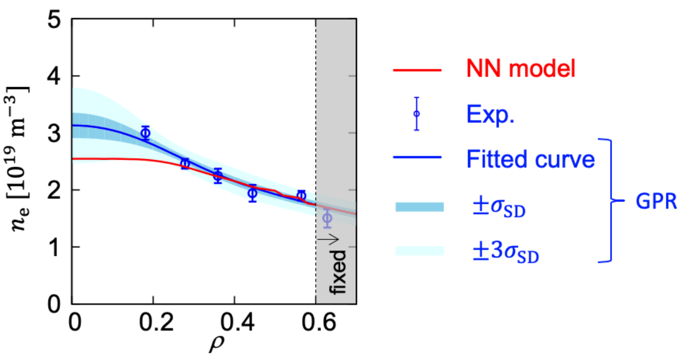

Figure 3. The predicted density profile for the plasma that is not included in the experimental dataset used for training of the NNs in comparison with the experimental profile.

Prediction of density profiles is performed with the integrated code TOPICS [11], that solves the electron particle transport equation using the turbulent particle flux given by the semi-empirical particle transport model. The reproducibility of the density profile with the developed model has been checked for a plasma that is not included in the dataset for NN construction. As shown in figure 3, the predicted n_{e} almost falls within the uncertainty band. In addition to density profile prediction, the diffusion and pinch terms are calculated individually. It has been confirmed that the difference in the diffusion and pinch terms between cases A and B shown in section 3 can be reproduced by the developed model.

References

[1] C. Angioni *et al.,* Phys. Rev. Lett. **90** 205003 (2003).

[2] H. Takenaga *et al.,* Nucl. Fusion **48** 075004 (2008).

[3] C. Angioni *et al.,* Nucl. Fusion **47** 1326 (2007).

[4] T. Tala *et al.*, *Proc. Int. Conf. on Fusion Energy (Ahmadabad, India, 2018)*, EX/4-4 (2018).

[5] E. Fable *et al.,* Plasma Phys. Control. Fusion **52**, 015007 (2010).

[6] J. Citrin *et al.,* Nucl. Fusion **55** 092001 (2015).

[7] O. Meneghini *et al.,* Nucl. Fusion **57** 086034 (2017).

[8] E. Narita *et al.,* Plasma Phys. Controlled Fusion **60**, 025027 (2018).

[9] A.G. Peeters and D. Strintzi Phys. Plasmas **11** 3748 (2004).

[10] A.G. Peeters *et al.,* Comput. Phys. Commun. 180 2650 (2009).

[11] N. Hayashi and the JT-60U team Phys. Plasmas 17 056112 (2010).

Effects of Electron Cyclotron Heating on the Toroidal Flow in Helical Plasmas

Yasuhiro YAMAMOTO, Sadayoshi MURAKAMI, Ching-Chieh CHANG, Santhosh T.A. KUMAR[1)], Joseph N. TALMADGE[1)], Konstantin LIKIN[1)] and David T. ANDERSON[1)]

Kyoto University, Kyoto 615-8450, Japan

[1)] *University of Wisconsin-Madison, Madison, Wisconsin 53706, USA*

The toroidal torque related to the electron cyclotron heating (ECH) is investigated in HSX plasma. Radial diffusion of energetic electrons by ECH makes the ion cancelling current and this ion current generates the $j \times B$ torque, which may play important role in the toroidal rotation observation during ECH in the HSX plasma. We investigate the energetic electron distribution by ECH applying GNET code, which can solve the 5D drift kinetic equation for the energetic electron. We evaluate the $j \times B$ torque and the the collisional torque due to the friction of the toroidal drift motion of energetic electrons. As a result, we obtained a significant torque due to the ECH and that the larger torque is obtained in Mirror configuration than that in QHS one. These results are consistent with the experiment observations.

1 Introduction

An important role of toroidal flow in the turbulence transport is suggested in many experiments. Recently, spontaneous toroidal flows in the electron cyclotron heating (ECH) plasma have been observed in many tokamak and helical devices, e.g. JT-60U, LHD and HSX. It has been required to make the mechanism clear and many studies have been done experimentally[1] and theoretically[2].

The Helically Symmetric Experiment (HSX) is the first quasi-symmetric stellarator device. There are two typical configurations of HSX. One is Quasi Helical Symmetry (QHS) configuration, which has the helical direction of symmetry in $|B|$. The $(m, n) = (1, 4)$ mode in Boozer spectrum is dominant in QHS configuration. Another one is Mirror configuration, where a set of auxiliary coils makes toroidal mirror terms, $(0, 4)$ and $(0, 8)$ modes, to the magnetic field spectrum in order to break the symmetry.

The flow measurement experiments have been done in HSX with the charge exchange recombination spectroscopy (CXRS)[3]. QHS configuration makes neoclassical viscosity smaller than that of Mirror configuration because of the helical symmetry, and so we can expect that toroidal flow velocity in QHS configuration would be larger than that in Mirror configuration. However, smaller toroidal flow has been observed in the QHS configuration. It has not been understood well yet.

In this study, we evaluate the the direction and strength of torques by ECH using GNET code[4], which can solve a linearlized drift kinetic equation in the 5D phase-space, and discuss what makes the difference.

2 Theory and simulation model

In order to study about ECH, we apply GNET code, which can solve the drift kinetic equation in 5-D phase space using Monte Carlo method. We split the gyrophase averaged electron distribution function, f, into a stationary part, $f_{\rm Max}$, and oscillating part by ECH, δf, as $f = f_{\rm Max} + \delta f$, where we consider the stationary part is Maxwellian. The drift kinetic equation for δf is given by

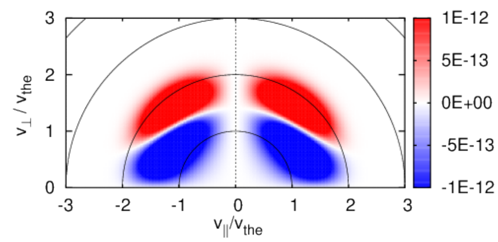

Fig. 1 The quasi-linear diffusion term of ECH.

$$\frac{\partial \delta f}{\partial t} + (\vec{v}_d + \vec{v}_{\parallel}) \cdot \frac{\partial \delta f}{\partial \vec{r}} + \dot{v} \cdot \frac{\partial \delta f}{\partial \vec{v}} - C(\delta f) - L(\delta f) = S^{\rm ql}(f_{\rm Max}) \quad (1)$$

where $\vec{v}_{\parallel}$ and $\vec{v}_d$ are the parallel velocity to the magnetic field and the drift velosity. Also, $C(\delta f)$, $L(\delta f)$ and $S(f_{\rm Max})$ are the collision operator, the orbit loss term, and the quasi-linear diffusion operator as the source term for the absorption of ECH, respectively.

The ECH driving term is discribed by the quasi-linear diffusion theory. We consider that interaction between the EC waves and particles are so long that the plasma can reach the steady state. Here we ignored the quasi-linear effect, $S^{\rm ql}(\delta f)$, in the quasi-linear diffusion source term for simplicity. Since we evaluate the torque by ECH in the steady state, we assume that the density and the temperature are constant. Under these conditions, the source term

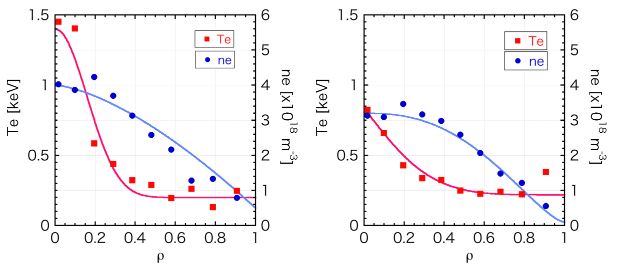

(a) QHS (b) Mirror

Fig. 2 The experimental data of the density and the electron temperature. The plots are experimental data, and the lines are fitting of them. In simulations, the fitting profiles are used.

S^{ql} is given by[6]

$$S^{\text{ql}}(f_{\text{Max}}) = -\delta(\vec{r} - \vec{r}_0) \cdot \frac{\partial}{\partial v_i} D^{\text{ql}}_{ij} \frac{\partial f_{\text{Max}}}{\partial v_j} \tag{2}$$

where D^{ql}_{ij} is the quasi-linear diffusion tensor, and $\vec{r}_0$ is the heating position obtained by ray tracing code. The fundamental O-mode ECH is applied in HSX. One typical case of the quasi-linear source term is shown in Fig.1. It shows the heating from blue region to red region.

ECH can drive the radial electron current j_{e}. The net current in steady state should vanish to maintain the quasi-neutrality, so the return current, $j_{\text{b}}(= -j_{\text{e}})$, must flow in the bulk plasma. Therefore, the bulk plasma feels $j_{\text{b}} \times B$ torque.

On the other hand, the supra-thermal electrons drift toroidal due to the precession motion in the direction opposite to the $j_{\text{e}} \times B$ torque. During the slowing down of supra-thermal electrons, they transfer their momentum to the bulk plasma due to collisions. If we consider the isotopic source, the torque of the passing particles in Co direction cancels that of the passing particles in Counter direction. The trapped particles, however, have the precession motion, and it can make the net collisional torque. The two torques should cancel in the completely symmetric configuration[5]. However, non-symmetric magnetic modes enhance the radial electron flux and break the cancellation of the two torques.

3 Simulation Results

We perform the simulation assuming typical temperature, density and radial electric field of HSX ECH plasma as shown in Fig.2. The plasma parameters are as follows: the magnetic axis major radius $R_{\text{ax}} \sim 1.2$ [m]; the averaged minor radius $a \sim 0.15$ [m]; toroidal magnetic field strength $B_{\text{T}} = 1.0$ [T]; the absorption power of ECH $P_{\text{abs}} = 100$ [kW].

Applying GNET code, we evaluate the velocity distribution of δf. Fig.3 (a) and (b) shows the velocity distribution at normarized minor radius $\rho \sim 0.1$ and 0.3 surface. The velocity distribution of total δf is shown in Fig.3 (c). They are the deviation from Maxwellian distribution, where the red region means the increasing and blue is decreasing. Energetic electrons can be found outer regions apart from the heating point. This result means that there is the radial electron flux as shown in Fig.4 .

HSX has the helical symmetry of (1,4) mode, and so we have to consider 2-dimensional torque as Fig.5. We cannot compare the size of vectors among three configuration because it is emphasized in order to make it easy to see. Also, we use the toroidal-poloidal angle as the axis, not $r\theta$ and $R\phi$, for simplicity. As a result, the total torque in completely symmetric configuration is almost perpendicular to the symmetry direction. However, even in QHS configuration, the $j \times B$ torque is much larger than the collisional torque, and the total torque has the component parallel to the helically symmetry direction. The direction of the parallel component is the same direction as the observed flow in the experiments. We consider that the symmetric conponent is important for the flow. Therefore, we evaluate the helical force, corresponding to the helical component of the torque, below.

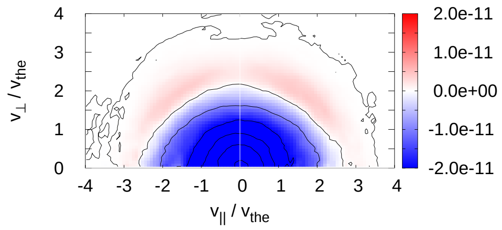

(a) $\rho \sim 0.1$

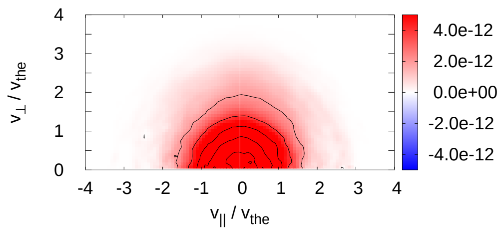

(b) $\rho \sim 0.3$

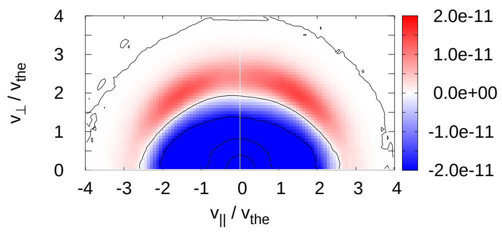

(c) The δf in the total δf.

Fig. 3 The velocity distribution of δf and the radial flux. They show the deviation from Maxwellian.

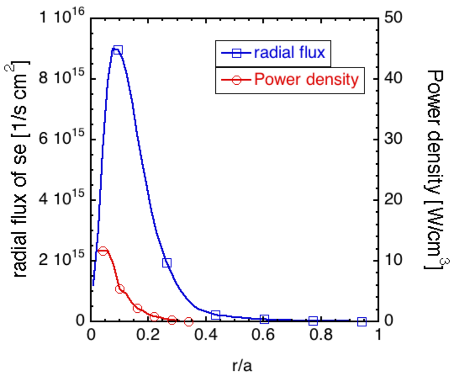

Fig. 4 The radial flux profile of supra-thermal electrons and the absorption power density.

Fig.6 shows the helical force in each configuration. In the completely helically symmetric configuration, the total force is quite small. Even QHS configuration has the net force of the symmetry direction. As noted above, the $j \times B$ force is dominant in QHS and Mirror configurations. Also, the torque in Mirror is larger than that in QHS configuration. This is consistent with the experiments.

In order to investigate the difference of the helical force and the radial orbit among these configurations, we calculate the collisionless drift orbit of the energetic electron with the energy $E = 5$keV and the pitch angle $\lambda \sim 20°$ (passing) or $80°$ (trapped). The orbit in each configuration is shown in Fig.7. As seen from Fig.7 (a), the orbits of a passing particle are the same among the three configurations, so the three orbits look like one line. However this is not the case for trapped particle. In the completely symmetric configuration, the helically trapped particle goes around and doesn't move radially. To the contrary, the particle goes radially in QHS configuration and the orbit in Mirror configuration is much larger than that in QHS configuration. The radial flux can be roughly understood as the radial mean free path, which is determined by the collision frequency and the radial drift velocity. When the collisionality is low enough for electrons to move along the drift orbit, larger orbit makes more flux. Therefore, the torque is much smaller in completely helically symmetric configuration, and that in Mirror configuration is larger than that in QHS configuration.

QHS configuration has not only the helically symmetric mode but also other non-symmetric modes. Also, Mirror configuration has two large non-symmetric magnetic modes additionally. The effect of non-symmetric modes is shown in Fig.8. In QHS configuration, 7 non-symmetric modes are $10 \sim 20\%$ of (1,4) mode near the axis ($\rho \sim 0.1$) and enhance the radial flux. When we ignore each magnetic mode one by one, the helical force decreases little by little. When all of the 7 modes are not including, the profile

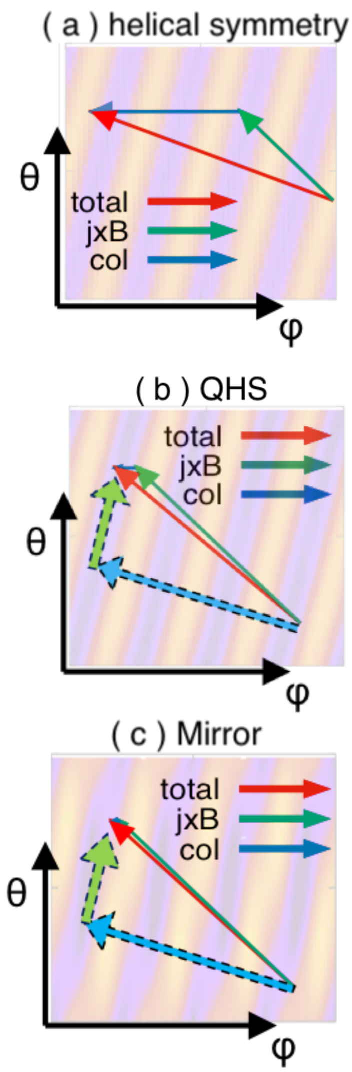

Fig. 5 The direction of each torque. (a) is that of the completely helically symmetric configuration, (b) is that of QHS configuration, and (c) is that of Mirror configuration. The green dashed vector is the component of helical symmetry direction, and the blue dashed vector is its perpendicular component. The background contour shows the magnetic field strength pattern.

is similar to that of the helical symmetriy case. Therefore we can consider that there is no especially dominant effective mode among them. In Mirror configuration, Mirror terms, (0,4) and (0,8) mode, dominate the enhancement of the radial flux. Except for the two Mirror modes, the helical force has very similar profile to that of QHS case.

4 Conclusions

We have evaluated the collisional and $j \times B$ torques by ECH, using GNET code. In axisymmetric and helically symmetric configuration, the collisional and $j \times B$ torques almost cancel each other in the direction of symmetry. QHS and Mirror configuration has the component of the symmetry direction. This symmetry direction is the same

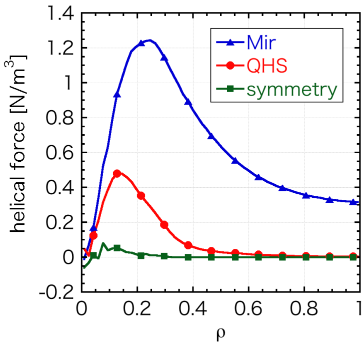

Fig. 6 The helical total force. They include $j \times B$ and collisional force.

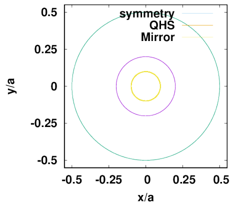

(a) Passing orbit.

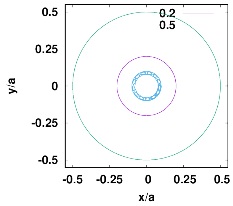

(b) Trapped orbit in the completely helically symmetric config.

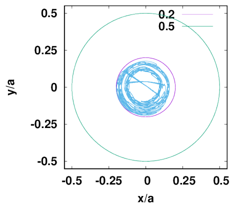

(c) Trapped orbit in QHS config.

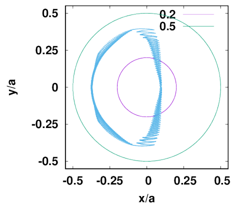

(d) Trapped orbit in Mirror config.

Fig. 7 The collisionless orbit of a supra-thermal electron. Fig. (a) shows the passing orbits of the three configurations and Fig.(b)-(d) shows each trapped orbit.

with the experimental flow direction, so we consider that helical force is important. As a result, we obtained the larger torque in Mirror configuration than that in QHS configuration. This result is consistent with the experimental observation. It is also found that what makes the dependence is the orbit enhanced by the non-symmetric magnetic mode.

In order to compare the simulation with the experiment, we must solve the momentum balance equations with viscosity and torque. Now we are tackling the flow calculation. In the neoclassical prediction, the flow should be small in the core region where the gradients are small. However large flow was observed in Mirror configuration. As a preliminary calculation, we solved them with some limitations and assumptions. The torque makes the parallel flow to the magnetic field line in the expected direction. Therefore ECH torque would explain the large flow in Mirror configuration.

[1] M. Yoshida, et al., Nucl. Fusion **49** (2009) 115028.
[2] P. H. Diamond, et al., Nucl. Fusion **53** (2013) 104019.

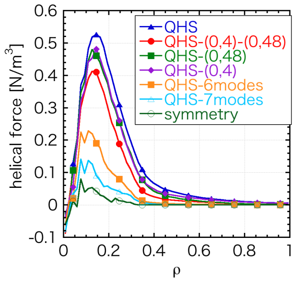

(a) QHS config.

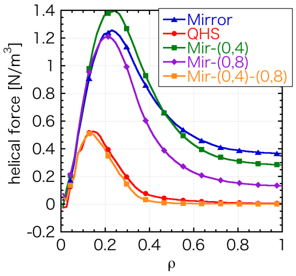

(b) Mirror config.

Fig. 8 The helical force profiles not including several modes (a) and (b).

[3] A. Briesemeister , et al., Plasma Phys. Control. Fusion **55** (2013) 014002.
[4] S. Murakami, et al., Nucl. Fusion **40** (2000) 693.
[5] M. N. Rosenbluth and F. L. Hinton, Nucl. Fusion **36** (1996) 55.
[6] M.Brambilla, Kinetic Theory of Plasma Waves Homogeneous Plasmas, Oxford Science Publications, 1998

Ion Mixing Mode Revisited

M. Yagi[1], K. Miki[1], N. Miyato[1], and B. Scott[†]

[1]QST, Rokkasho Fusion Institute
[†]IPP Garhing

Introduction

The particle transport is an important research topic for burning control in DEMO reactors. For example, the hollow density profile is often seen after pellet injection or gas-puff. In such a case, the inverted density gradient appears in the edge region which produces the particle pinch. To understand particle pinch mechanism, we have performed local gyrokinetic simulation using DEFEFI code[1, 2] with the positive density gradient ($dn/dr > 0$). We have observed inward particle flux for such condition. To understand the mechanism of particle pinch, we have revisited the ion-mixing mode theory proposed by B. Coppi[3]. It is pointed out that the electron drift wave contributes to the particle pinch rather than the ion-mixing mode for the inverted density gradient.

Simulation Results

Simulation parameters relevant to plasma edge in ASDEX Upgrade are used: $R_0 = 165$cm, $n_e = 2.0 \times 10^{13}$cm, $T_e = 100$eV, $L_n = -7$cm, $L_{T_i} = L_{T_e} = L_T = 3.5$cm, $T_i/T_e = 1$, $B = 2.5$T, $a/R = 0.303$, $L_\perp/R = L_T/R = 0.0212$, $q = 3.5$, $\beta = 6.44 \times 10^{-5}$, $\nu_i(L_\perp/c_s) = 9.56 \times 10^{-3}$, $\nu_e(L_\perp/c_s) = 8.23 \times 10^{-1}$. Here we assume $L_x = L_y$. Grid numbers and time step for simulation are given as $(n_x, n_y, n_z, n_w) = (32, 128, 32, 32, 16)$ and $\Delta t = 5 \times 10^{-3}$. Figure 1 shows the temporal evolution of particle flux for the cases with the normal density gradient $L_n = 7$cm and the inverted density gradient $L_n = -7$cm. It is seen that inward particle flux appears for $L_n = -7$cm. Figure 2 shows the dependence of mode frequency on wavenumber with $L_n = -7$cm. Here the negative sign corresponds to the electron diamagnetic frequency, since $\omega_{*e} < 0$ for $L_n < 0$.

Revisit of Ion Mixing Mode

A. Local Analysus

We assume the non-adiabatic electron response is written by $i\delta$ model as

$$\frac{\tilde{n}_e}{n_0} = \frac{e\tilde{\varphi}}{T_e}(1 + i\delta), \tag{1}$$

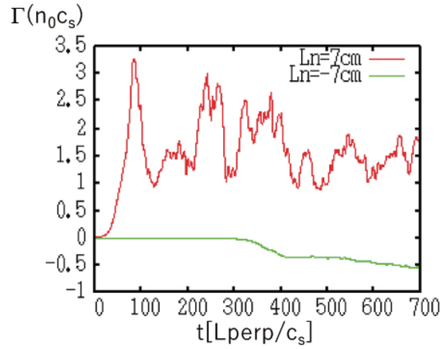

Fig.1 Temporal evolution of particle flux.

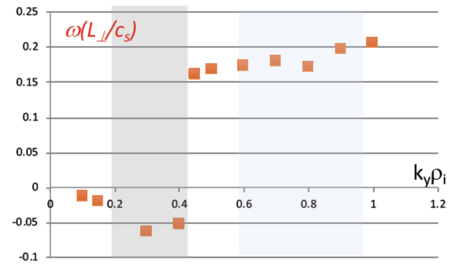

Fig.2 Dependence of mode frequency on wavenumber.

where

$$\delta = \frac{k}{\omega_\chi}\left(\omega - \omega_{*e} + \frac{3}{2}\omega_{*e}\eta_e\right), \tag{2}$$

$k = 1 + \alpha_T$, α_T the thermal force coefficient and $\omega_\chi = k_\parallel^2 v_{the}^2/\nu_e$. The quasi-linear particle flux is given by

$$\Gamma = \langle \tilde{n}\tilde{v}_{E\times B,r}\rangle = -\frac{2c}{B}\Im\left(\sum_{k_\theta>0} k_\theta \tilde{\varphi}_{k_\theta}\tilde{n}_{k_\theta}\right) = -2n_0 D_B^e \sum_{k_\theta>0}\delta k_\theta \left|\frac{e\tilde{\varphi}}{T_e}\right|^2, \tag{3}$$

where $D_B^e = cT_e/eB$. If $\delta > 0$, the $\Gamma < 0$ which means the inward particle flux.

we obtained the local dispersion relation of the ion-mixing mode including the toroidal ITG effect as

$$1 + i\delta - \frac{1}{\Omega} + \left(-\frac{k_\parallel^2 c_s^2}{\omega_{*e}^2}\frac{1}{\Omega^2} + b_s + \frac{2\epsilon_n}{\Omega}\right)\left(1 + \frac{K}{\Omega}\right) = 0, \tag{4}$$

where $K = (1+\eta_i)/\tau$, $b_s = (k_\theta\rho_s)^2$, $\epsilon_n = L_n/R$, and $\Omega = \omega/\omega_{*e}$. If we set $b_s = 0$ and $\epsilon_n = 0$ and assume $K \gg \Omega$, then the original model is obtained.

B. Nonlocal Analysis

Using the ballooning transformation and taking the strong ballooning limit, we obtain the eigenvalue equation as

$$\begin{aligned}&\frac{\partial^2}{\partial\chi^2}\left[\frac{c_s^2}{\omega_{*e}^2\Omega^2}\frac{1}{q^2R^2}\frac{\partial^2\phi}{\partial\chi^2} + B\phi + \left(b_s s^2 + \frac{2\epsilon_n}{\Omega}\left(s - \frac{1}{2}\right)\right)\chi^2\phi\right]\\ &-i\frac{k}{A}\frac{\nu_e\omega_{*e}}{v_e^2}(\hat{\eta}_e + \Omega)q^2R^2\phi = 0,\end{aligned} \tag{5}$$

where

$$\hat{\eta}_e \equiv 1.5(\eta_e - 1.5), \quad A \equiv 1 + \frac{K}{\Omega}, \quad B \equiv \left(1 - \frac{1}{\Omega}\right)\frac{1}{A} + b_s + \frac{2\epsilon_n}{\Omega}, \tag{6}$$

and $-\infty \ll \chi \ll +\infty$. This equation is solved by the Hermite expansion and the dispersion relation is given by

$$b_s \left(\frac{q\Omega}{\epsilon_n}\right)^2 \left\{\left(1-\frac{1}{\Omega}\right)\frac{1}{A} + b_s + \frac{2\epsilon_n}{\Omega}\right\}^2 + \left(b_s s^2 + \frac{\epsilon_n(2s-1)}{\Omega}\right)$$
$$\times \left\{2n+1+i\frac{2}{2n+1}\frac{k}{A}\frac{\nu_e\omega_{*e}}{v_e^2}q^2R^2\frac{\hat{\eta}_e+\Omega}{b_s s^2+\epsilon_n(2s-1)/\Omega}\right\}^2 = 0. \tag{7}$$

For the simulation parameter, $K=-1$, so that we can derive the simplified dispersion relation. We consider two limits. In the case of $b_s\Omega \ll 2\epsilon_n$,

$$\Omega(\Omega+2\epsilon_n)^2 + \overline{s}\left(2n+1+i\frac{\overline{\nu}}{2n+1}\frac{\Omega^2(\Omega+\hat{\eta}_e)}{\Omega-1}\right)^2 = 0, \tag{8}$$

where

$$\overline{s} = \frac{\epsilon_n^3}{b_s q^2}(2s-1), \quad \overline{\nu} = \frac{2k}{\epsilon_n(2s-1)}\frac{\nu_e\omega_{*e}}{v_e^2}q^2R^2. \tag{9}$$

For $\overline{\nu}=0$ and $b_s \ll 1$,

$$\Omega^3 + 4\epsilon_n\Omega^2 + 4\epsilon_n^2\Omega + \overline{s}_* = 0, \tag{10}$$

where $\overline{s}_* = \overline{s}(2n+1)^2$. This dispersion describes ITG mode with the special limit with $K=-1$. If we set $\overline{s}_*=0$, we have $\Omega=-2\epsilon_n$ which implies the toroidal ITG mode is marginal. On the otherhand, if we set $\epsilon_n=0$, the slab ITG mode is found to be unstable. In the case of $\Omega \gg 2\epsilon_n$ and $b_s \ll 1$,

$$(\Omega+\epsilon_n^*)(\Omega-1)^2 - \nu_e^{*2}\Omega(\hat{\eta}_e+\Omega)^2 = 0, \tag{11}$$

where

$$\epsilon_n^* \equiv \frac{\epsilon_n(2s-1)}{b_s s^2}, \quad \nu_e^* \equiv 2k\frac{\nu_e L_T/c_s}{\omega_{*e}L_T/c_s}\frac{m_e}{m_i}\frac{q}{\epsilon_n\hat{s}}, \quad \hat{s}=(2n+1)s. \tag{12}$$

This dispersion implies that the electron drift wave is destabilized by the non adiabatic electron response though the parallel electron heat conductivity for the inverted density gradient. This is another branch which can drive the inward particle flux in this limit. Figure 3 and 4 show mode frequency and linear growth rate given by the general dispersion relation Eq.(7). Here we use $k_\theta\rho_s = 0.3$, $s=1$, other parameters are same as those used in the nonlinear simulation. For comparison, those given by Eqs.(10) and (11) are also shown by the label wr(ITG) and wr(EDW), respectively. Good agreement between Eq.(7) and Eqs.(10), (11) is obtained. Here $\Omega_i < 0$ corresponds to unstable mode since $\omega_{*e} < 0$. From Figures (3) and (4), we conclude the electron drift wave plays a crucial role for the particle pinch for the inverted density gradient limit rather than the ion-mixing mode.

For summary, The ion-mixing mode is revisited in the case of inverted density gradient taking account of toroidai curvature. It is shown that there exists two unstable modes, namely, the ion-mixing mode and the electron drift wave. The ion-mixing mode is driven by negative compression (slab ITG mode) and non-adiabatic electron response though parallel electron heat conductivity. The toroidal effect is subdominant. For the case with the inverted density gradient, the electron drift wave is dominant which produces the particle pinch. As future work, ion mode should be identified which is observed in high k_θ regime.

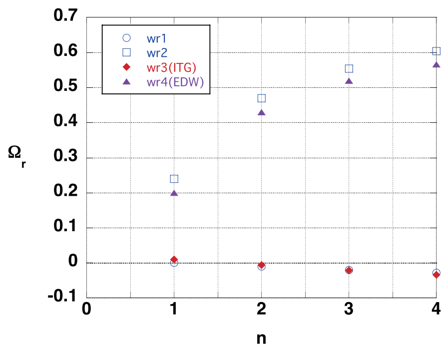

Fig.3 Dependence of mode frequency on radial quantum number n.

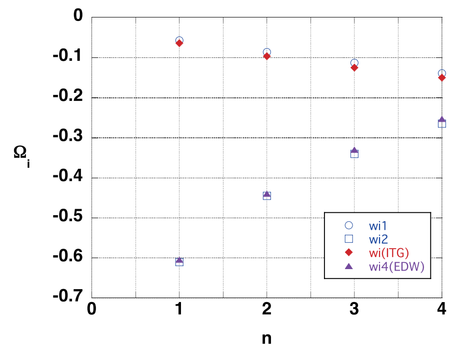

Fig.4 Dependence of growth rate on radial quantum number n.

References

[1] B. Scott, Phys. Plasmas 17 (2010) 102306.

[2] K. Miki, N. Miyato, B. Scott, M. Yagi, Proc. of M&C 2017, Korean Nuclear Society, 2017-01.

[3] B. Coppi and C. Spight, Phys. Rev. Lett. 41 (1978) 551.

Role of density modulation in driving nonlinear streamer flows in drift wave turbulence

Y. Kosuga[1,2]

[1] Research Institute for Applied Mechanics, Kyushu University, Fukuoka, Japan

[2] Research Center for Plasma Turbulence, Kyushu University, Fukuoka, Japan

Convective cells - nonlinearly generated ExB vorticities - play important roles in the nonlinear dynamics of turbulent plasmas. As they are linearly unstable, convective cells are nonlinearly driven from primary drift wave turbulence. There are two important limits of convective cells. One is a radially elongated cell, which is called a streamer. The other is a poloidally elongated cells, and is called a zonal flow. Since streamer and zonal flow have different impact on turbulent transport, it is a critical issue to understand their selection rule[1,2]. In order to selectively excite one flow or another, we must understand their generation mechanisms in detail.

In this work, we discuss the role of density modulation in streamer flows[3]. In the previous studies, modulational feedback from shearing was discussed. This mechanism is applicable to both zonal flows and streamers. In this process, shearing flows modulate underlying turbulence, which modulate the wave number of underlying turbulence. This leads to the amplification of the modulating flows. For the case of streamers, in addition to this process, we show that density modulation opens a novel feedback mechanism to amply the original flow. Unlike zonal flows, streamer has a finite poloidal mode number. As a consequence, streamer flows modulate density field. With this effect, the frequency of the underlying drift wave turbulence is modulated, which leads to the modulation of the poloidal wave number, very much like the wave number modulation in Langmuir turbulence. The relative importance of the shearing modulation and density modulation is evaluated, and for typical plasma parameters, the density modulation becomes dominant effect. With this density modulation feedback, we have revisited the selection rules of streamers and zonal flows. We find that streamer flows are selected i.) for the medium value of $\rho_* \sim 1/200 - 1/300$ and small fluctuation amplitude $\tilde{n}/n_0 < 1\%$ or ii.) large level of fluctuation amplitudes $\tilde{n}/n_0 < 10\%$ and $\rho_* \sim 1/10$. Thus streamer flows can be driven in the core region of the medium size tokamaks, or the linear machine such as PANTA.

Stimulating discussion with S. Inagaki, F. Kin, M. Sasaki, P.H. Diamond, K. Itoh, S.-I. Itoh, is acknowledged. This work was supported by Grants-in-Aid for Scientific Research of JSPF of Japan (JP15H02155, JP17H06089, JP18K03578), the Joint research project in RIAM.

References

[1] S. Champeaux and P.H. Diamond, Phys. Lett. A **288** 214 (2001)

[2] Y. Kosuga, Phys. Plasmas **24** 122305 (2017)

[3] Y. Kosuga and K. Hasamada, Phys. Plasmas **25** 100701 (2018)

Gyrokinetic simulation study of parity dependence of magnetic transport

G.J. Choi[1], B.J. Kang[1], T.-H. Watanabe[2] and T.S. Hahm[1]

[1] *Department of Nuclear Engineering, Seoul National University, Seoul, Korea*
[2] *Department of Physics, Nagoya University, Nagoya, Aichi, Japan*

1. Introduction

In the past, physics study of influence of finite plasma β on transport of magnetic fusion plasmas has been focused on linear stabilization of ion temperature gradient (ITG) modes [1,2] and onset of kinetic ballooning mode (KBM) [3] above critical β. The finite-β stabilization of ITG modes is well known to originate from magnetic field line bending [4]. More recently, considerable attention has been paid to finite-β effect on transport in fully nonlinear stage [5,6]. Nonlinear electromagnetic gyrokinetic simulations have showed that magnetic heat transport induced by electromagnetic ITG turbulence make non-negligible modification to heat flux. Parity analyses of the electromagnetic ITG turbulence have showed that nonlinearly generated tearing parity modes play an important role in magnetic heat transport [7] by making full stochasticity of fluctuating magnetic field [8], and thus significantly change β-dependence of electron magnetic heat flux. In this work, we perform a further detailed study of the parity dependence of magnetic heat transport of finite-β tokamak plasmas in ITG mode regime, analyzing results of nonlinear electromagnetic gyrokinetic simulations.

2. Nonlinear magnetic heat flux

Previously performed parity analysis of tokamak transport in ITG mode regime [7] showed that tearing parity modes, nonlinearly generated from linearly unstable twisting parity ITG modes, have significant contributions to electron magnetic heat flux. Following previous works, we analyzed results of nonlinear electromagnetic gyrokinetic simulations with cyclone base case parameters performed using GKV code [9]. Full-kinetic electron with real mass ratio was assumed, and $\beta_e = 0.6\%$ was chosen for the simulations. We obtained nonlinear electron and ion magnetic heat fluxes by averaging their amplitudes over the fully nonlinear stage. Fig. 1 shows k_y components of electron and ion nonlinear magnetic heat fluxes, each decomposed

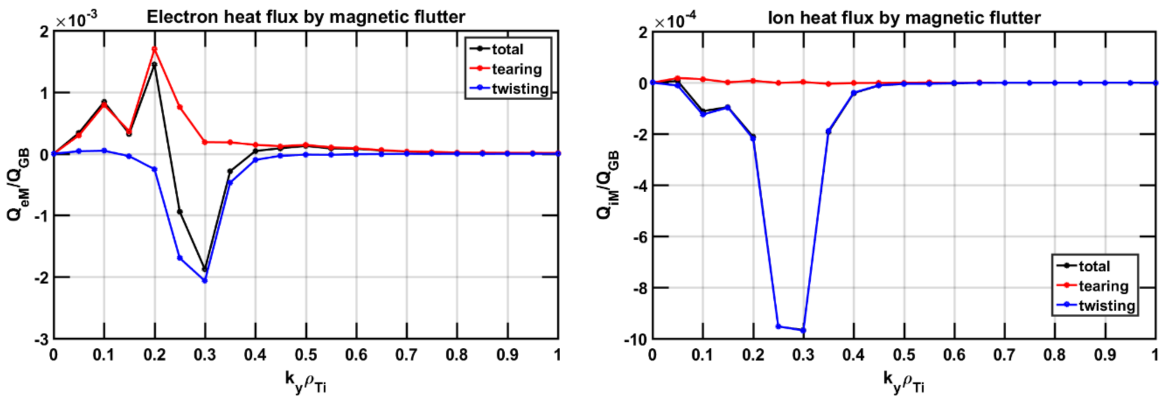

Fig. 1. GKV simulation results for k_y components of electron (left) and ion (right) magnetic heat fluxes (for $k_x = 0$ the most linearly unstable k_x) in nonlinear stage.

by parity of fluctuating radial magnetic field. First of all, the most linearly unstable mode ($k_x = 0,\ k_y\rho_i = 0.3$) has twisting parity and it induces inward magnetic heat flux, which partially cancels with electrostatic part and therefore results in reduction of net outward heat flux. Other twisting parity modes also induce inward magnetic flux. Meanwhile, nonlinearly generated tearing parity modes induce outward magnetic heat flux, which is unfavorable to tokamak confinement. Also, note on obvious disparity between electron and ion magnetic heat transport. The tearing parity modes give significant contributions to electron magnetic heat flux, but their contributions are negligible for the case of ion magnetic heat flux. Further quantitative analysis

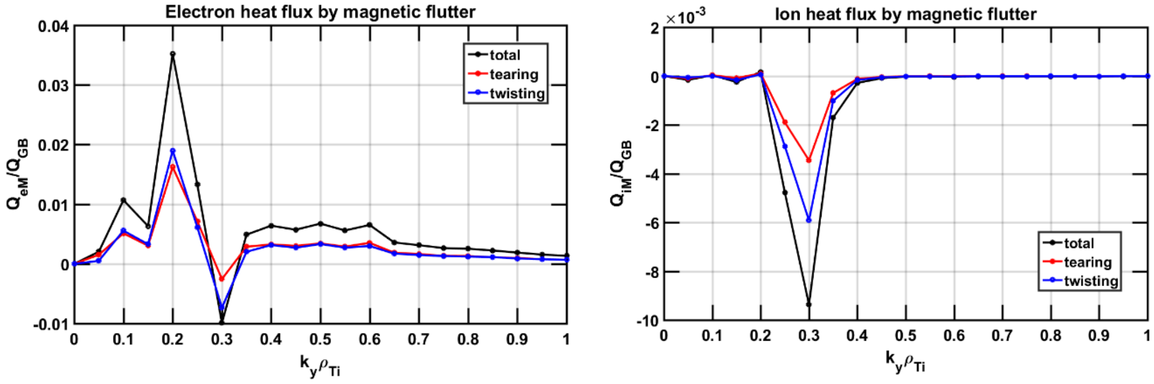

Fig. 2. GKV simulation results for k_y components of electron (left) and ion (right) magnetic heat fluxes (after summation over k_x) in nonlinear stage.

revealed that tearing parity modes make magnetic heat flux more efficiently than twisting parity modes for electron transport, while it is the opposite for ion transport. Fig. 2 shows heat fluxes containing contributions from all k_x components. It also shows significant contributions from nonlinearly generated modes on electron magnetic heat flux and negligible contributions for ion transport. However, the disparity between twisting and tearing parity significantly weakens. Further analysis and physical interpretation on this is ongoing.

3. Time evolution of magnetic heat flux

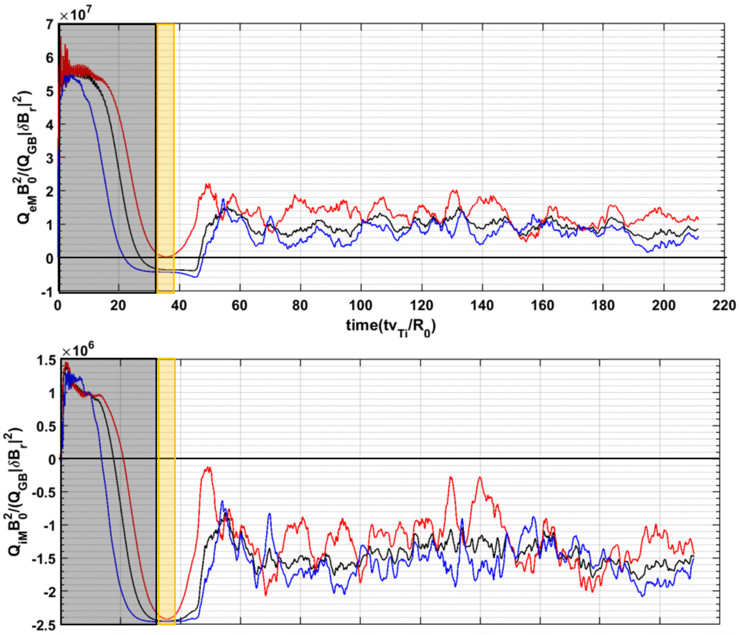

Fig. 3. GKV simulation results for time-evolution of electron (upper) and ion (lower) magnetic heat fluxes (after summation over k_x and k_y), normalized by square of radial magnetic field.

We also compared nonlinear magnetic heat fluxes to quasi-linear ones. Fig. 3 shows time evolution of electron and ion magnetic heat fluxes. It is clear that normalized nonlinear heat flux is more than normalized quasi-linear heat flux for electron magnetic transport. Also, the direction of electron nonlinear heat flux is opposite to that of quasi-linear heat flux. The trend is the reverse for ion magnetic transport; normalized nonlinear heat flux is less than normalized quasi-linear heat flux. Once again, clear disparity between electron and ion magnetic transport is revealed.

References

[1] W. Horton *et al*, Phys. Fluids **28**, 3050 (1985).

[2] B.G. Hong and W. Horton, Phys. Fluids B **1**, 1589 (1989).

[3] W.M. Tang, J.W. Connor and R.J. Hastie, Nucl. Fusion **20**, 1439 (1980).

[4] F. Jenko and W. Dorland, Plasma Phys. Control. Fusion **43**, A141 (2001)

[5] S.E. Parker *et al*., Phys. Plasmas **11**, 2594 (2004)

[6] M.J. Pueschel and F. Jenko, Phys. Plasmas **17**, 062307 (2010)

[7] D.R. Hatch *et al*., Phys. Rev. Lett. **108**, 235002 (2012)

[8] W.M. Nevins *et al*., Phys. Rev. Lett. **106**, 065003 (2011)

[9] T.-H. Watanabe and H. Sugama, Nucl. Fusion **46**, 24 (2006)

Stable structure of hydrogen in tungsten di-vacancy and its isotope effect

Kazuhito Ohsawa[1], Takeshi Toyama[2], Yuji Hatano[3], Masatake Yamaguchi[4], Hideo Watanabe[1]

[1]Research Institute for Applied Mechanics, Kyushu University
[2] Institute for Materials Research, Tohoku University
[3]Hydrogen Isotope Research Center, University of Toyama
[4]Center for Computational Science and e-system, Japan Atomic Energy Agency

1. Introduction

Divertor armor tiles installed in fusion reactors are exposed to intense plasma particle irradiation. So, the divertor armor tiles are covered by tungsten (W) or its alloys because they have excellent properties as plasma facing materials (PFMs), e.g., low hydrogen (H) solubility, high melting point and high mechanical toughness etc. However, a large amount of H isotopes (D and T) retention has been reported in the tungsten materials. In particular, tritium inventory is an important subject associated with safety of fusion reactors. H isotopes are not retained in perfect crystal lattice of W because of its low H solubility. However, H isotopes can be accommodated in vacancy-type lattice defects nucleated by plasma particle irradiation. Stable structures of multiple H atoms trapped in a W mono-vacancy have been reported in our previous work [1]. In the present work, we pay attention to stable structures of H atoms trapped in W di-vacancy. Besides, the isotope effects are investigated by taking into account zero point energy (ZPE) of H atoms.

2. Methodology

Stable structures of multiple H atoms trapped in the di-vacancy are investigated in terms of first-principle calculations on the basis of density functional theory. The calculations are performed by using Vienna ab initio simulation package (VASP) with PBE type potential. The cut-off energy of plane wave is 350eV. We use large supercell composed of 432 lattice points ($6\times6\times6$ BCC lattice) in the present calculations in order to reduce the effects of periodic boundary condition imposed on the supercell. Lattice relaxations are iterated until resultant force of each atom is lowered than 0.003 eV/Å.

The binding energies of H atoms to the di-vacancy not including ZPE corrections are defined by

$$E_b = E[\mathrm{V}_2] + kE[\mathrm{H}^{\mathrm{I}}] - E[\mathrm{V}_2\mathrm{H}_k], \qquad (1)$$

where E is the cohesive energy of the corresponding supercell; V_2, H^{I}, and $\mathrm{V}_2\mathrm{H}_k$ indicate di-vacancy, interstitial H atom, and di-vacancy trapping k H atoms, respectively. The ZPEs of H atoms are calculated by harmonic oscillation approximation, that is, the forces acting on the H atoms in stable structures are assumed to be proportional to the displacement from the equilibrium positions. The binding energies including ZPE correction are

$$E_b^Z = E_b + kZ\left[\mathrm{H^I}\right] - Z\left[\mathrm{V_2H}_k\right], \tag{2}$$

where Z means the total ZPE of H atoms in the corresponding supercell.

3. Results

We investigate stable structure of di-vacancy in W lattice. First nearest neighbor configuration, that is, two vacancies line up in the <111> direction, is most stable. H atoms trapped in the di-vacancy are located in the vicinity of octahedral interstitial sites (O-sites) on the inner surface of the di-vacancy, as shown in Fig. 1. There are 12 O-sites next to the di-vacancy. Besides, the O-sites are classified into two types. Six O-sites located in the interface area of the di-vacancy are represented by red numbers. While, six O-sites located in the periphery area are expressed by

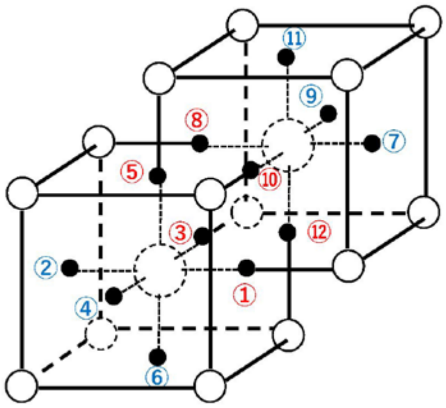

Fig. 1 Di-vacancy in the first nearest neighbor configuration and O-sites next to the di-vacancy.

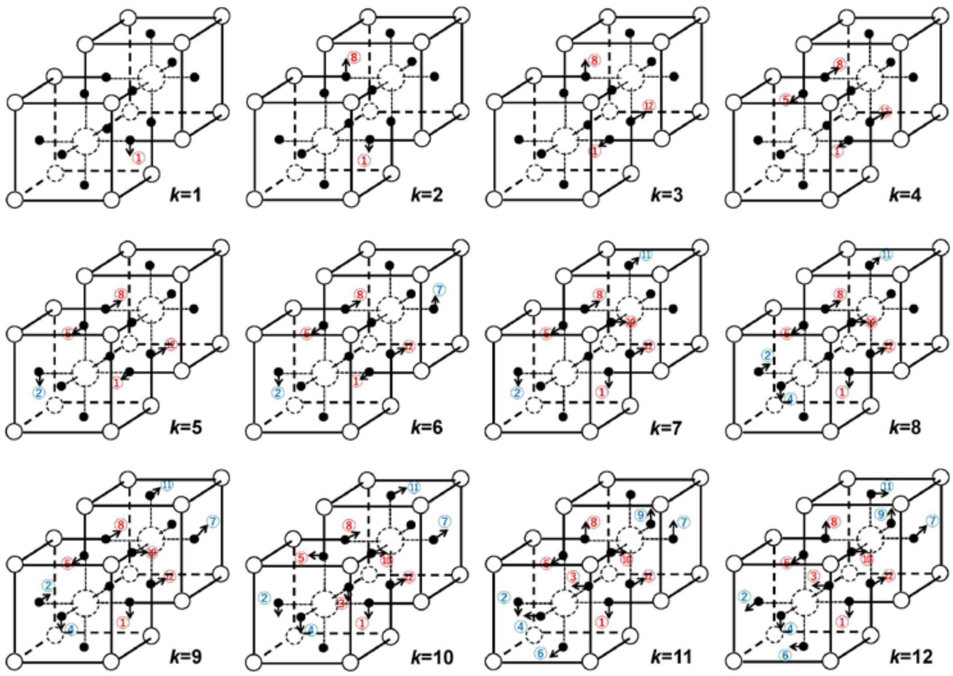

Fig.2 Stable structures of H atoms in W di-vacancy. k indicates the number of H atoms trapped in the di-vacancy. Each H atoms occupying O-site is represented by red or blue number corresponding to the O-site. The arrows indicate the displacement directions of H atoms from the O-sites.

blue numbers, as shown in Fig. 1. Stable structures of H atoms trapped in W di-vacancy not including ZPE corrections are shown in Fig. 2. The H atoms preferentially occupy the O-sites in the interface area when the number of H atoms in the di-vacancy is less than five. While, H atoms occupy the O-sites located in the periphery area as H atoms increase. Stable structures of H atoms not including and including ZPE corrections are not always identical, as shown in Fig. 3. The dependence of the binding energy on the number of H atoms trapped in the di-vacancy is exhibited in Fig. 4. The binding energies including ZPE corrections E_b^Z are larger than those not including ZPE corrections E_b.

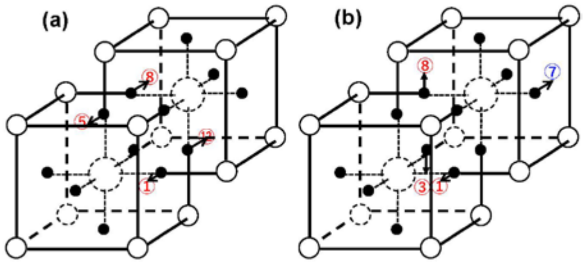

Fig. 3: Stable structures of four H atoms in the di-vacancy (a) not including and (b) including ZPE corrections, respectively.

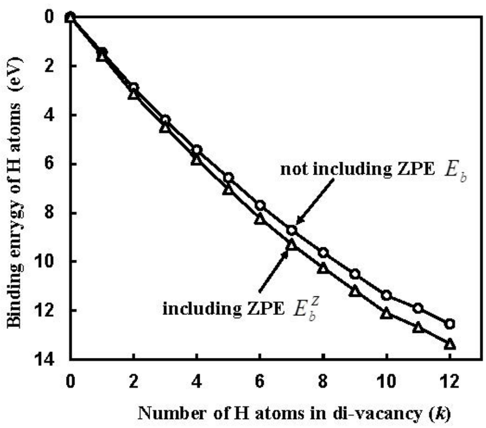

Fig. 4: Binding energies of H atoms not including E_b and including E_b^Z ZPE corrections.

4. Discussion

The affiliation of H atoms to the O-sites in the interface area is larger than that in the periphery area. However, mutual repulsive interaction acts on the H atoms. Actually almost all H atoms are displaced from O-sites so as to keep distance each other, as shown in Fig. 2. The stable structures of H atoms are supposed to be determined by the balance of the affiliation and repulsive interaction. Furthermore, the stable structures of H atoms and the binding energies are affected by the ZPEs of H atoms. According to Fig. 4, we find that $E_b < E_b^Z$, i.e. ZPE causes the increment of the binding energies. The lighter H isotopes have larger ZPE. Therefore, the lighter H isotopes are supposed to be trapped in the vacancy-type lattice defects more than the heavier ones.

References

[1] K. ohsawa *et al.*, Phys. Rev. B 85 (2010) 184117.

Kinetic simulations for particle transport of multi-species plasmas in LHD

Masanori Nunami

National Institute for Fusion Science, Toki 509-5292, Japan

Using gyrokinetic and drift-kinetic simulations, we investigate the anomalous and neoclassical particle transport of multi-species plasma in Large Helical Devise. In a high ion temperature plasmas including the carbon impurity ion with hollow density profile, the gyrokinetic simulations within wide ranges of radial gradients of temperatures and densities represent that the turbulent contributions of particle fluxes are varied satisfying the ambi-polar condition between multi-ion-species and electron. And the turbulent contribution of the impurity carbon particle flux remains radially inward directed. For the neoclassical contributions, the drift-kinetic simulations indicate that neoclassical particle fluxes of ions can change due to ambi-polar radial electric field and the external momentum sources. The external torques of injected heating beam cause not only the ion-root, but also the electron-root. In the case of electron-root, the neoclassical contributions of the particle fluxes may be balanced with the turbulent contributions obtained from gyrokinetic simulations.

1 Introduction

For designing of fusion reactors, physics of the plasma heat and particle transport is one of the critical issues in fusion plasma researches. Numerical approaches via gyrokinetics and drift-kinetics frameworks are useful to make progress in the researches. In the multi species Large Helical Devise (LHD) [1] plasmas heated by neutral beam injection (NBI), we often observe the extremely hollow density profile of impurity ions, which is called impurity hole. It is one of the advantages for fusion reactors because the impurity hole structure may avoid the impurity accumulations which exacerbate core plasma performances. Therefore, the understandings of the impurity hole generations are strongly demanded for magnetically confined plasma researches. In the multi-species plasmas, the particle transport fluxes should satisfy the balance relations for the species s,

$$\frac{\partial n_s(\rho)}{\partial t} + \frac{1}{V'}\frac{\partial}{\partial \rho}V'\left(\Gamma_s^{(\mathrm{NC})} + \Gamma_s^{(\mathrm{Trb})}\right) = \mathcal{S}_s. \tag{1}$$

If the system is in the steady state, $\partial n_s/\partial t = 0$, and the auxiliary particle sources and sinks can be negligibly small, $\mathcal{S}_s \sim 0$, the neoclassical contribution of the particle transport fluxes

author's e-mail: nunami.masanori@nifs.ac.jp

$\Gamma_s^{(\mathrm{NC})}$ should be balanced with the turbulent contributions $\Gamma_s^{(\mathrm{Trb})}$ for each species s, namely $\Gamma_s^{(\mathrm{NC})} \sim \Gamma_s^{(\mathrm{Trb})}$. Therefore, in this work, the neoclassical and turbulent contributions to the particle transport of the plasma are investigated based on the gyrokinetic and drift-kinetic frameworks.

2 Turbulent particle fluxes

From here, we consider the impurity hole LHD plasma which consists of four species (e, H, He, C). We perform the gyrokinetic turbulence simulations using the GKV code [3, 4] in order to evaluate turbulent contributions of the plasma transport. In the previous linear estimates in the plasma, it was found that the ion temperature gradient (ITG) mode is a dominant instability [5]. From the nonlinear simulations with wide ranges of temperature gradients of ions and electron within 50% changes from their nominal values, it is found that the particle transport fluxes have quite different temperature gradient dependences between different particle species. Furthermore, the impurity carbon particle flux remains negative, namely radially inward-directed.

In addition to the temperature gradients, the density gradient lengths for several particle species also affect the particle transport fluxes. Figure 1 shows the density gradient dependences of the turbulent particle fluxes for each species. In the results, it is found that there are quite different dependences. The density gradients of bulk ions (H and He) have little impacts on each particle flux. In contrast, the density gradients of electron and carbon ion strongly affect the turbulent particle fluxes of electron and hydrogen. However, for the carbon particle flux, it cannot be radially outward-directed unless the impurity hole structure is disappeared, in which the carbon density profile becomes to be peaked.

Therefore, at least in the results from the temperature and density gradient dependences, the turbulent contribution of the carbon particle flux is inward-directed, and the neoclassical particle flux of carbon is demanded to be outward-directed to balance with the turbulent contribution.

3 Neoclassical particle fluxes

For the simulations to evaluate the neoclassical contributions of the particle transport in the impurity hole LHD plasma, we employ the DKES/PENTA code [6]. In our previous work [7], due to the external torque from the NBI heating on the neoclassical fluxes, the co-injected external torque can cause not only ion-root with negative ambi-polar radial electric field E_{r} but also electron-root with positive E_{r}. In the case of the electron-root, each neoclassical particle flux is changed from the ion-root case. Especially, the intensities of the particle fluxes are moderated, and $-\Gamma_s^{(\mathrm{NC})}$ close to the turbulent contributions $\Gamma_s^{(\mathrm{Trb})}$ obtained by gyrokinetic simulations, i.e., $\Gamma_s^{(\mathrm{NC})} + \Gamma_s^{(\mathrm{Trb})} \sim 0$. Therefore, if the impurity hole LHD plasma is in the electron-root, the particle balance relation, Eq.(1) may be satisfied within the kinetic frameworks.

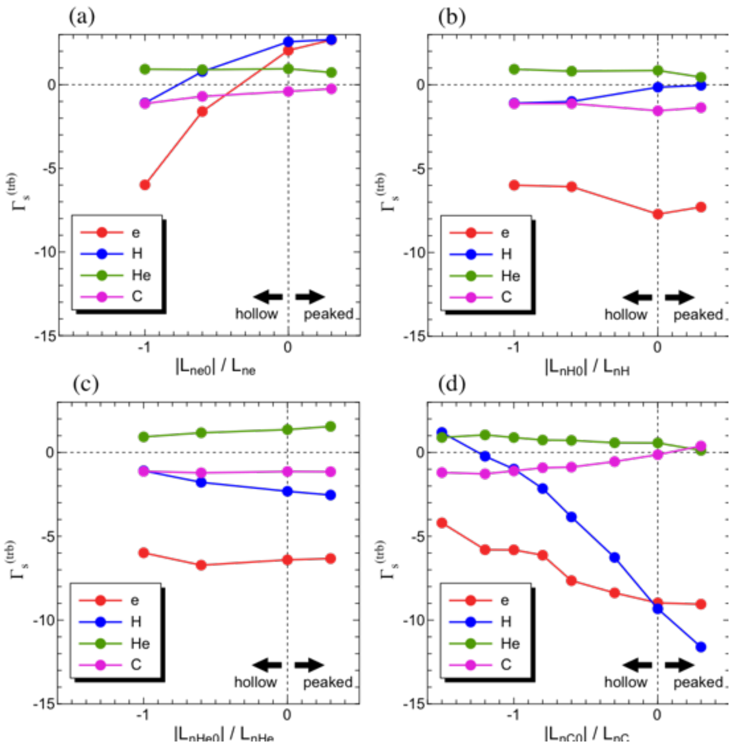

Fig. 1 Turbulent particle fluxes for changing (a) electron density gradient, (b) hydrogen density gradient, (c) helium density gradient, and (d) carbon density gradient. Here, each fluxes are evaluated at r/a = 0.6 and normalized by the arbitrary unit.

Acknowledgment

This work is supported in part by the RIAM collaborative Research Program (30FP-12), JSPS KAKENHI (16K06941 and 18H01202), NIFS Collaborative Research Program (KNTT043, KNTT045 and KNST095), and by FLAGSHIP2020, MEXT within the priority study 6. The results were obtained by using the K computer at the RIKEN (hp170260, hp180200 and hp180083), JFRS-1 at IFERC CSC (KML3D, GKVISO and GT5DSTL), and "Plasma Simulator" at NIFS.

[1] Y. Takeiri, *et al.*, Nucl. Fusion **57**, 102023 (2017).
[2] M. Nunami, *et al.*, 26th IAEA FEC, TH/P2-3 (2016).
[3] T.-H. Watanabe and H. Sugama, Nucl. Fusion **46**, 24 (2006).
[4] M. Nunami, T.-H. Watanabe, and H. Sugama, Plasma Fusion Res. **5**, 016 (2010).
[5] M. Nunami, *et al.*, 27th IAEA FEC, TH/P6-8 (2018).
[6] D.A. Spong, Phys. Plasmas **12**, 056114 (2005).
[7] M. Nunami, *et al.*, Plasma Fusion Res. **12**, 1203039 (2017).

Analysis of energetic particle confinement in LHD using neutron diagnostics and Fokker-Planck codes

H. NUGA[1], R. SEKI[1,2], K. OGAWA[1,2], S. KAMIO[1], Y. FUJIWARA[1], M. OSAKABE[1,2], M. ISOBE[1,2], T. NISHITANI[1], M. YOKOYAMA[1,2], and LHD Experiment Group

[1]National Institute for Fusion Science, Toki, Japan
[2]SOKENDAI (The Graduate University for Advanced Studies), Toki, Japan

Introduction The physics of the fast ion transport is the one of the important issue for the achievement of the magnetically confined fusion reactor. This is because the plasma temperature is sustained by the kinetic energy transfer from fast ions generated by external heatings and fusion born alpha particles. For this reason, the fast ion transport mechanism has been investigated in several magnetic confinement devices and simulations. Since the fast ion transport is governed by several mechanisms, however, the accurate prediction of the fast ion transport is difficult. In out research, we estimate the fast ion confinement time from the measurements and simulations in the Large Helical Device (LHD) instead of the theoretical approach.

The neutron measurements in deuterium plasmas play an important role to estimate the fast ion confinement time. In present fusion devices, such as LHD, the fusion reaction between thermal and non-thermal ions is dominant instead of thermal-thermal fusion reaction. For this reason, we can survey the fast ion density profile and the fast ion velocity distribution from the neutron measurements.

To investigate the fast ion confinement time, a series of the short-pulse neutral beam (NB) injection experiment has been performed in LHD. The decay time of the fusion born neutron emission rate has been observed after the NBs have been turned off. There are two factors which cause the neutron emission rate decaying. One is the reduction of the fusion cross-section due to the fast ion slowing down. The other factor is the reduction of the fast ion density due to the fast ion transport. Since the contribution of the fast ion slowing down can be estimated by simulation codes, the differences between experiment and simulation results shows the contribution of the fast ion transport. In this paper, we investigate the fast ion confinement time by using LHD experiment data and simulation codes.

Experiment scenario Figure 1 shows the typical waveform of this series of experiment. NB port-through power and energy, electron density and temperature on axis, and the neutron emission rate are displayed. In this experiment, three tangential NBs (NB#1-#3) and a perpendicular NB (NB#4) are used. Four NBs (NB#1-#4) have the pulse width of 40 ms. Plasmas are sustained by 2.5 MW electron cyclotron heating system.

Analysis tools The neutron emission rate is simulated by using FIT3D code[1, 2] and CONV_FIT3D code. FIT3D calculates the fast ion birth profile including the finite orbit width effect. CONV_FIT3D calculates the slowing down of NB fast ions. This code solves the fast ion slowing down equation based on the classical Coulomb collision theory. Since the energy distribution of NB fast ions can

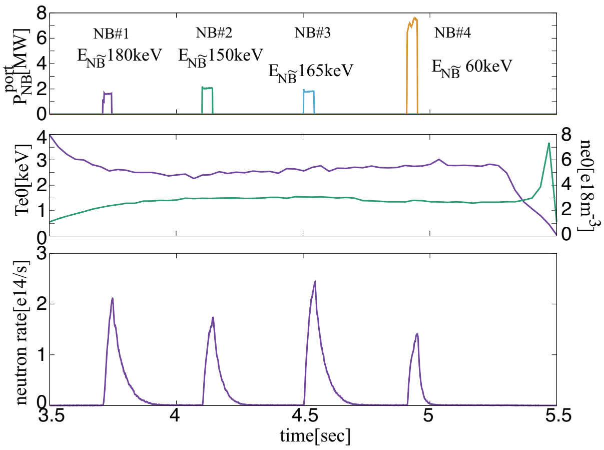

Figure 1: Typical waveform of this series of experiment (SN139605).

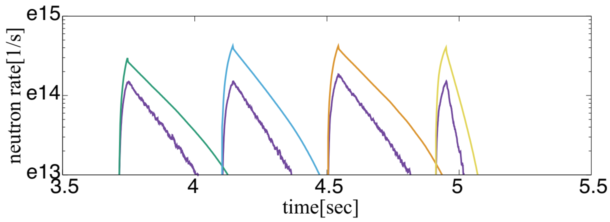

Figure 2: Time evolutions of measured and simulated neutron emission rate (SN139599).

be obtained by CONV_FIT3D, the time evolution of the neutron emission rate can be also estimated. The deuterium-deuterium fusion cross section is approximated by the beam-thermal fusion dominant model derived by Ref. [3]. In addition, the coefficients of the astrophysical S function is chosen from Ref. [4].

As noted above, the decay of the neutron emission rate comes from two factors; the fast ion slowing down and the fast ion transport. Therefore, the measured neutron decay time τ_n^{exp} can be described as:

$$(\tau_n^{\mathrm{exp}})^{-1} = (\tau_n^{\mathrm{sim}})^{-1} + \tau_c^{-1}, \tag{1}$$

where, τ_n^{sim} and τ_c indicate the simulated neutron decay time and the fast ion confinement time, respectively. Since the present simulation ignores the fast ion transport, the fast ion confinement time can be estimated from the differences between measured and simulated neutron decay time.

In the following calculation, it is assumed that the plasma species is pure deuteron, the effective charge $Z_{\mathrm{eff}} = 1$ and $T_e = T_i$. The neutron decay time is not sensitive to the effective charge though the neutron emission rate is sensitive to the plasma effective charge. This is because the contribution from the fast deuteron-electron Coulomb collision is dominant to the slowing down of NB fast ions. From our previous investigation[5], it can be considered that these assumptions are valid to the present calculation.

Analysis Result Figure 2 is the example of the time evolution of the measured and simulated neutron emission rate. Since the simulation ignores the fast ion transport, it is found that the simulated neutron decay time is longer than the measured neutron decay time. Figure 3 shows the relation between measured and simulated neutron decay time. It is found that as simulated neutron decay time increases, the measured neutron decay time separates from the simulated value due to the presence of τ_c. The fast ion confinement time in each beam, which are displayed in fig. 3, can be obtained by least-square fitting method in $\tau_n^{\mathrm{exp}} = \tau_n^{\mathrm{sim}}\tau_c/(\tau_n^{\mathrm{sim}} + \tau_c)$. From fig. 3, it is found that the perpendicular NB fast ions have a poor confinement than the tangential NB fast ions. This can be explained by the strong ripple induced particle diffusion in LHD.

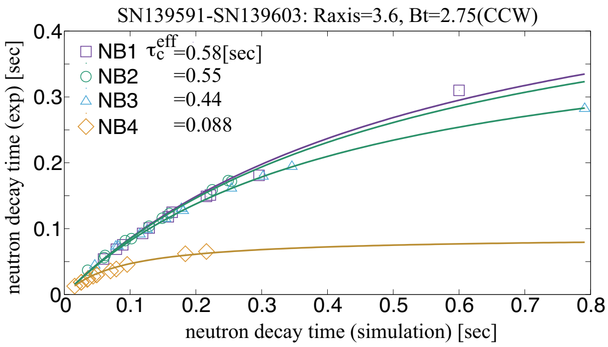

Figure 3: The measured neutron decay times are plotted against the simulated neutron decay times.

Conclusion In this paper, to investigate the fast ion confinement in LHD, a series of experiments and simulations have been performed. We estimate the fast ion confinement time from the differences between measured and simulated neutron decay time. The fast ion confinement time is obtained by the least-square fitting method. From this estimation, the confinement time of tangential NBs have approximately $\tau_c \sim 0.5$ sec and the confinement time of perpendicular NB has approximately $\tau_c \sim 0.09$ sec. In the present paper, we have estimated the fast ion confinement time in single magnetic configuration. The investigation of the dependence of the confinement time to the magnetic configuration is future works.

[1] S. Murakami, *et al.*, Fusion Technology **27** Suppl., (1995).
[2] P. Vincenzi, *et al.*, Plasma Physics and Controlled Fusion **58**, 125008, (2016).
[3] D. Mikkelsen, Nucl. Fusion **29**, 1113, (1989).
[4] H. -S. Bosch, G. Hale, Nucl. Fusion **32**, 611, (1992).
[5] H. Nuga, *et al.*, Nucl. Fusion **59**, 016007, (2019).

Modelling of heat transport in LHD using neural network with non-dimensional input parameters

S. Maeta, S. Murakami, H. Yamaguchi, A. Fukuyama, K. Nagaoka[a], H. Takahashi[a], H. Nakano[a], M. Osakabe[a], K. Tanaka[a], M. Yokoyama[a], and LHD Exp Group[a]

Department of Nuclear Engineering, Kyoto University, Kyoto 615-8540, Japan
[a]National Institute for Fusion Science,322-6 Oroshi-cho, Toki 509-5292, Japan

introduction

Various physical phenomena with wide ranges of time and space scales are connected in the fusion plasma. Thus, in order to predict the performance of the fusion plasma, an integrated simulation combining various physics models is required. Many integrated simulation code has been developed for tokamak and helical plasmas. TASK3D is an integrated simulation code for helical plasma and has been applied to the analyses of the plasma transport of LHD plasmas[1, 2].

In the previous study, TASK3D is assumed that the transport coefficients are given as the sum of neoclassical (NC) and turbulent (TB) transport coefficients. The integrated heat and particle transports simulation of NBI heating plasma of LHD had been previously performed and this simulation result had been compared with experimental result. The result shows that simulation result is good agreement some experimental result when the turbulence transport model of ion is gyro-Bohm(gradT) model and of electron is gyro-Bohm model[1, 2]. However, more experiments are performed in LHD, and simulation result of TASK3D is not good agreement with other some experimental result. It is considered that there are regions of plasma parameters that can not be reproduced in the turbulence transport models. Therefore, a heat transport model that is in good agreement with many experimental results of different plasma parameters in LHD is necessary.

In LHD, more experiments are performed than those shots, and a database of experiments using TASK3D-a has been constructed. Studies to model transportation from many LHD experimental data have been done. By modeling the thermal diffusion coefficient χ from the experimental data by statistical method, good agreement with χ of the experiment was obtained[3]. In addition, the heat flux Q using neural network(NN) is also predicted for the experimental data of DIII-D[4].

In this paper, we construct NN that predicts direct heat flux Q without considering neoclassical transport and turbulent transport components. We also verified the parameters affecting the result of the constructed NN using the sensitivity analysis method.

Modeling of heat flux using Neural Network

Simulation model

we use database in the range of $r/a < 0.9$ and the database accumulated by TASK3D-a. This research is a collaborative research with Dr. Yokoyama and we share the data set[3]. We selected 18 non-dimentional input parameters(Table1). In this study, we evaluated the performance of NN using RMSE and RMSPE for error. We divided the data into training, test, validation data and evaluated NN by cross validation method. First, we learned NN using training data so that RMSE between Q_{NN} predicted from neural network (NN) and experimental value $Q_{exp}(= Q_i, Q_e)$ is minimized. In order to prevent over fitting to training data, we stored the weights and biases of NN when RMSE becomes minimum on validation data. Finally, we calculated RMSE for test data which we did not use for training and evaluated the performance of the model against unknown data. We constructed NN for electron and ion respectively. nality normalized by Banana-Plateau boundary

Table 1: input parameter of NN

Expression	Name
R/a	Normalized major radius
r/a	Normalized mainor radius
T_e/T_i	Ion to electron temperature ratio
$n_e a^3$	Normalized electron density
$\frac{1}{T_i}\frac{dT_i}{d\rho}$	Ion temperature scale length
$\frac{1}{T_e}\frac{dT_e}{d\rho}$	Electron temperature scale length
$\frac{1}{n_e}\frac{dn_e}{d\rho}$	Electron temperature scale length
q	Safety factor
$\frac{dq}{d\rho}$	Normalized safety factor shear
$\epsilon_{eff}^{1.5}$	
ν_{ep}^*	Electron collisionality normalized by Plateau-PS boundary
ν_{ip}^*	Ion collisionality normalized by Plateau-PS boundary
ν_{eh}^*	Electron collisionality normalized by $1/\nu$-Plateau boundary
ν_{ih}^*	Ion collisionality normalized by $1/\nu$-Plateau boundary
ν_{eb}^*	Electron collisionality normalized by Banana-Plateau boundary
ν_{ib}^*	Ion collisionality normalized by Banana-Plateau boundary
ρ_e^*	Normalized electron Larmor radius
ρ_i^*	Normalized ion Larmor radius

Simulation result

Fig.1 on the left is the regression plots of comparing heat flux of NN results and experimental results and shows a good agreement with experimental results. Fig.1 on the right is histograms and shows good statistical agreement of the NN model for train and validation data but histograms for test data has larger error than other data. The RMSE of ion and electron for test data are 0.029 and 0.031. RMSE for training and validation data is smaller than test data, and the value of NN model prediction is good agreement with experimental results for all data(training, validation, test).

Fig.2 shows the RMSPE values of the sensitivity analysis results. We have also verified the main variables for predicting heat flux in NN using sensitivity analysis. As sensitivity analysis, we have verified how the output changes by increasing the value of the input parameter by 10 to 40%. As a result of the sensitivity analysis of the ions, RMSPE is in the order of largeness: R/a, T_e/T_i, $n_e a^3$, which indicates that this is the main component of NN. The sensitivity analysis of our NN model has shown no strong

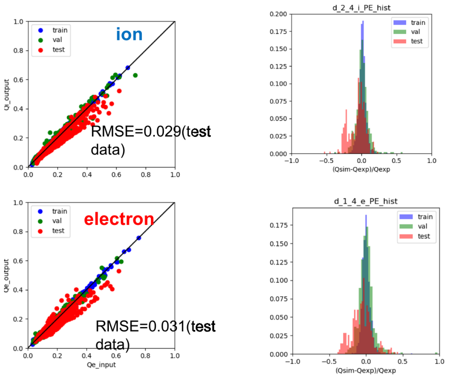

Figure 1: On the left is regression plots of comparing heat flux of NN results and experimental results. On the right is histogram of ion and electron

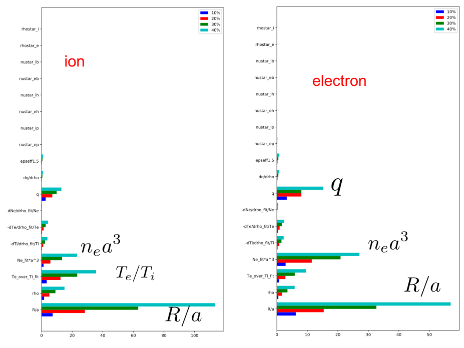

(a) ion (b) electron

Figure 2: The results of electron and ion sensitivity analysis

dependency of the variable in the gyro-Bohm model and OLS analysis. As a result of the sensitivity analysis of the electron, RMSPE is in the order of largeness: R/a, $n_e a^3$, q, which indicates that this is the main component of NN.

Summary

We have studied the heat flux of ion and electron in LHD using NN. The developed NN model of ion and electron has shown a good agreement with experimental results. The RMSE for test data of ion is 0.029 and of electron is 0.031. We have also verified the main variables for predicting heat flux in NN using sensitivity analysis. The sensitivity analysis of our NN model has shown no strong dependency of the variable in the gyro-Bohm model. We will analyze important variables affecting heat transport by decreasing input variables and analyzing sensitivity.

References

[1] S. Murakami, et al., Plasma Phys. Control. Fusion **57** (2015) 054009.

[2] A. Sakai, et al., Plasma Fusion Res. **9** (2014) 3403124.

[3] M. Yokoyama, Plasma and Fusion Research **9** (2014) 1302137.

[4] O. Meneghini,Physics of Plasmas **21** (2014) 060702.

Integrated simulation study of LHD type fusion reactor by TASK3D

T. Shinogi, S. Murakami, S. Maeta

Department of Nuclear Eng., Kyoto Univ., Nishikyo, Kyoto 615-8540, Japan

1 Introduction

Design research of a helical fusion reactor is underway based on the present large helical device (LHD). In the previous studies, they verify the plasma operation scenario for the LHD-type helical reactor FFHR-d1 in view of MHD equilibrium/stability, neoclassical transport, α-particle energy loss and impurity effect. Moreover, they identify a self-consistent solution of the plasma operation scenario which achieves steady-state sustainment of the burning plasma with a fusion gain of $Q \sim 10$ is found in the operation regime that has been already confirmed in LHD experiment. They study FFHR-d1 with simple turbulent diffusion coefficients which is several times neoclassical diffusion coefficients. It is necessary to study with more accurate turbulent transport models.

In this study, we investigate the possibility of a steady state only by α-particle heating, that is $Q = \infty$, in the LHD type reactor. We assume LHD type fusion reactor, LHR4, whose size is four times larger than LHD and whose magnetic field strength is 5[T]. Moreover, we assume turbulent diffusion models which are agree with results of LHD experiment in TASK3D.

2 Simulation model

We assume the LHD type fusion reactor, LHR4, which is 4 times larger in the size scale than those of LHD. Table 2 shows the comparisons of the configuration parameters for LHD and LHR4.

We apply the integrated transport simulation code, TASK3D, to study the stated sate of LHDR4. TASK3D is the integrated transport code for helical plasma based on TASK code and has been developed in collaboration between Kyoto Univ. and NIFS. TASK3D is composed of multiple modules each modeling one physical phenomenon. One dimensional diffusion transport module (TR module) mainly used in this research calculates heat and particle transports of plasma by solving one dimensional diffusion equations. The diffusion coefficient in TASK3D is defined as the sum of neoclassical diffusion coefficient and turbulent diffusion coefficient as $\chi_s = \chi_s^{\mathrm{NC}} + \chi_s^{\mathrm{TB}}$, where subscript s represents particles. Turbulent transport model has been studied to reproduce results of LHD experiments. One of models is the gyro-Bohm type for electron, which is given by

$$\chi_{\mathrm{e}} = C_{\mathrm{gB}} \frac{T_{\mathrm{e}}}{eB} \frac{\rho_{\mathrm{i}}}{a}$$

	Major radius [m]	Minor radius [m]	Magnetic field strength [T]
LHD	3.6	0.632	5.0
LHR4	14.4	2.528	2.75

Table 1: Comparisons of the configuration parameters of LHD and LHR4

and is the gyro-Bohm-gradT type for ion, which is

$$\chi_{\mathrm{i}} = C_{\mathrm{gBgT}} \frac{T_{\mathrm{e}}}{eB} \frac{\rho_{\mathrm{i}}}{a} \left(\frac{\Delta T}{T} a \right).$$

These turbulent transport model for electron and ion reproduce well the results of LHD experiments. The other model is the one proportional to the inverse of plasma density, which is given by

$$\chi_{\mathrm{e,i}} = C_{1/n} \frac{10^{19}}{n_{\mathrm{e,i}}},$$

where C_{gB} , C_{gBgT} and $C_{1/n}$ are constant which show good match with results of experiments in previous research. In this study, we investigate the steady state of the LHR4 assuming these two turbulent models.

For simplicity, we solve only the evolution of the ion and electron temperature, and the plasma density is fixed in this study. We assume three type of density profiles shown in figure 1.

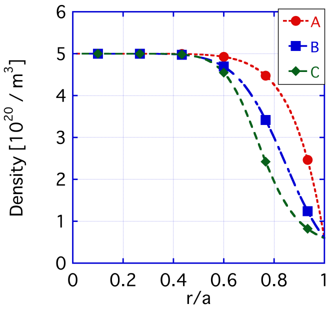

Figure 1: Plasma density profile A, B and C. ($n(0) = 5.0 \times 10^{20}/\mathrm{m}^3$)

We introduce constant coefficient F_{NC} and F_{TB} for neoclassical heat diffusion coefficient and turbulent diffusion coefficient. Thus, we assume heat diffusion coefficient as

$$\chi_s = F_{\mathrm{NC}} \cdot \chi_s^{\mathrm{NC}} + F_{\mathrm{TB}} \cdot \chi_s^{\mathrm{TB}}.$$

F_{NC} and F_{TB} show how much transportations are reduced from the current models. In the future operation of the nuclear fusion reactor, it is heated up by neutral beam incidence (NBI) heating and raised, and the temperature is raised by plasma heating. However, in this study, we start simulation with enough high temperature ($11 \sim 21$keV) to sustain nuclear fusion reaction. We do not consider external heating and only α particle heating is assumed as a heat source ($Q = \infty$) in this simulation. We change F_{NC} from 10^{-3} to 1, F_{TB} from 10^{-3} to 1, central density $n(0)$ from 1.0 to 6.0 $\times 10^{20}[\mathrm{m}^{-3}]$, and initial central temperature from 11 to 21keV.

3 Results

First, we assume the gyro-Bohm-gradT model. We vary initial temperatures of ion and electron to investigate the dependence of central temperature at steady state : $T_{\mathrm{s}(e,i)}$ with initial temperature. The time evolution of the central temperature reaching the steady state is shown in figure 2. We assume following parameters; $F_{\mathrm{NC}} = 1$,$F_{\mathrm{TB}} = 0.1$, $n(0) = 5.0 \times 10^{20}[\mathrm{m}^{-3}]$ and B density profile. We show the typical case where the steady state is not achieved with same condition as

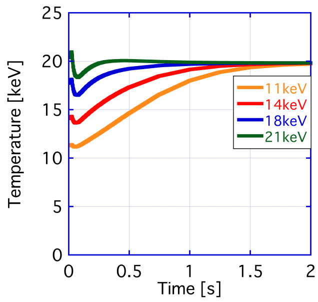

Figure 2: Time evolution of electron central tmperature changing initial temperatures with $F_{\mathrm{TB}} = 0.1$ (Steady state)

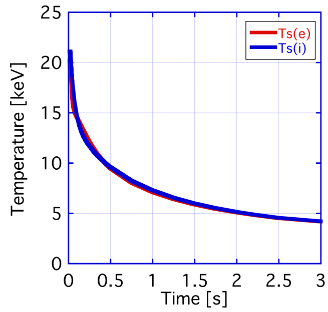

Figure 3: Time evolution of electron and ion central temperature with $F_{\mathrm{TB}} = 0.3$

above except F_{TB}. In figure 3, $F_{\mathrm{TB}} = 0.3$ is. We have found that in gyro-Bohm-gradT model, $T_{\mathrm{s(e,i)}}$ reaches almost the same temperature (about 20keV) with $F_{\mathrm{TB}} = 0.1$ even when the initial temperature is changed. In the case of $F_{\mathrm{TB}} = 0.3$, we do not achieve steady state against any initial temperature.

We fix the constant coefficient of neoclassical component $F_{\mathrm{NC}} = 1$ and change that of turbulent component F_{TB}, $n(0)$, density profiles to investigate dependence of $T_{\mathrm{s(e,i)}}$ with them. Figure 4 shows dependence of $T_{\mathrm{s(e,i)}}$ with F_{TB} and $n(0)$ with B density profile. The solid line represents the electron central temperature at steady state $T_{\mathrm{s(e)}}$ and dashed line represents that of ions. Figure 5 shows dependence of $T_{\mathrm{s(e,i)}}$ with density profiles with $F_{\mathrm{TB}} = 0.1$. The higher the central density

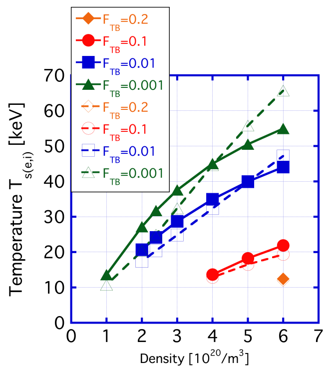

Figure 4: Density dependence of $T_{\mathrm{s(e,i)}}$ with $F_{\mathrm{NC}} = 1$ changing F_{TB}

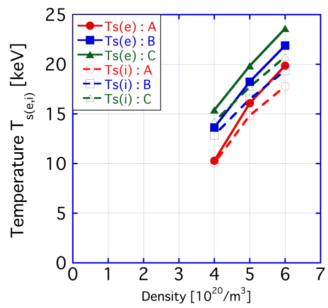

Figure 5: Density dependence of $T_{\mathrm{s(e,i)}}$ in several density profiles (A, B and C) with $F_{\mathrm{NC}} = 1, F_{\mathrm{TB}} = 0.1$

becomes, steady state is also achieved for higher F_{TB} value. We found that $T_{\mathrm{s(e,i)}}$ is highest with C density profile.

We changed the value of F_{NC} in order to consider the case that we could improve the neoclassical transport more than the current LHD. We fix $F_{\mathrm{TB}} = 0.1$ and change F_{NC} from $10^{-3} \sim 1$ in three density profiles. Figure 6 shows dependence of $T_{\mathrm{s(e,i)}}$ with F_{NC} and $n(0)$ with B density profile. The effect of lowering the order of F_{NC} is smaller than the influence of F_{TB}. This is because heat transport of electrons is dominated by turbulent transport. We show plots of $T_{\mathrm{s(i)}}$

with various F_{NC} and F_{TB} in B density profile and$n(0) = 5.0 \times 10^{20}[\text{m}^{-3}]$ in figure 7. In figure 7, crossmark represents the condition when the steady state is not reached.

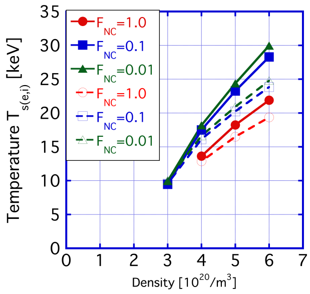

Figure 6: Density dependence of $T_{\text{s(e,i)}}$ with $F_{\text{TB}} = 0.1$ changing F_{NC}

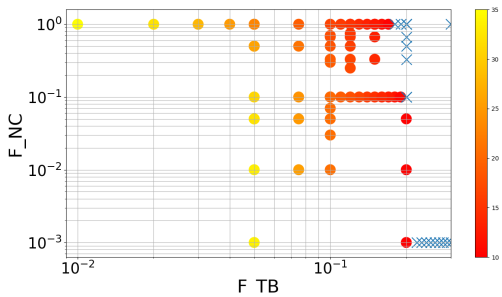

Figure 7: Dependence of $T_{\text{s(i)}}$ with F_{NC} and F_{TB}. The color of the markers show the temperature of $T_{\text{s(i)}}$.Cross marks show unsteady state conditions.

Then, we simulate with $1/n$ model. We fix $F_{\text{NC}} = 1$ and change $n(0)$ and F_{TB} from $10^{-1} \sim 1$ in three density profiles. Figure 8 shows the dependence of $T_{\text{s(e,i)}}$ with F_{TB} and density with B density profile and $F_{\text{NC}} = 1$. In $1/n$ model, we achieve the steady state $F_{\text{NC}} = 1$ and $F_{\text{TB}} = 1$. We show the dependence of $T_{\text{s(e,i)}}$ with density profiles in figure 9. we found that Changes in the density of near the boundary do not affect the central temperature at the steady state in $1/n$ model.

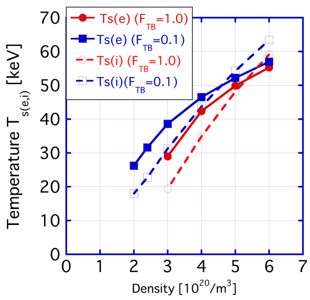

Figure 8: Density dependence of $T_{\text{s(e,i)}}$ with $F_{\text{NC}} = 1$ changing F_{TB} ($1/n$ model)

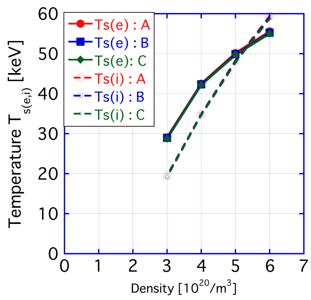

Figure 9: Density dependence of $T_{\text{s(e,i)}}$ in several density profiles (A, B and C) with $F_{\text{NC}} = 1, F_{\text{TB}} = 1$ ($1/n$ model)

4 Conclusion

We have investigated the possibility of a steady state only with α-particle heating, $Q = \infty$, in the LHD type reactor.

We assume the LHD type fusion reactor, LHR4, whose device size is four times larger than that of LHD and the magnetic field strength is 5[T] at the plasma center. We assume turbulent diffusion models which can reproduce well the results of LHD experiment. We have applied the integrated transport simulation code, TASK3D, to study the steady state of LHDR4. The diffusion coefficient in TASK3D was defined as the sum of neoclassical diffusion coefficient and turbulent diffusion coefficient as $\chi_s = \chi_s^{\mathrm{NC}} + \chi_s^{\mathrm{TB}}$, where subscript s represented particles. Turbulent transport model has been studied to reproduce results of LHD experiments. One of models was gyro-Bohm-gradT model, the other model was $1/n$ model. In this study, we have investigated the steady state of the LHR4 assuming these two turbulent models.

We have introduced constant coefficient F_{NC} and F_{TB} and assumed heat diffusion coefficient as $\chi_s = F_{\mathrm{NC}} \cdot \chi_s^{\mathrm{NC}} + F_{\mathrm{TB}} \cdot \chi_s^{\mathrm{TB}}$. F_{NC} and F_{TB} have shown how much transportations has been reduced from the current models. We did not consider external heating and only α particle heating was assumed as a heat source ($Q = \infty$) in this simulation.

We have found that in gyro-Bohm-gradT model, $T_{\mathrm{s(e,i)}}$ has reached almost the same temperature (about 20keV) with $F_{\mathrm{TB}} = 0.1$ even when the initial temperature has been changed. In gyro-Bohm-gradT model, we achieved steady state with $F_{\mathrm{NC}} = 1, F_{\mathrm{TB}} = 0.28$ in the high density. On the other hand, in $1/n$ model, we achieved the steady state with $F_{\mathrm{NC}} = 1, F_{\mathrm{TB}} = 1$.

From now on, we will study with finite Q value.

References

[1] A.Sagara,et al., Fusion Engineering and Design 89 (2014)

[2] T.Goto,et al., Nuclear Fusion Volume57 Number6 (2017)

[3] S.Murakami,et al., PlasmaPhys.Control.Fusion57 (2015)

Integrated Transport Simulation of LHD Plasma Applying Data Assimilation

Yuya Morishita, Sadayoshi Murakami, Masayuki Yokoyama[1], Genta Ueno[2]

Kyoto University, NIFS[1], The Institute of Statistical Mathematics[2]

1 Introduction

Data assimilation is one of forms of machine learning and has been developed mainly in meteorology and oceanology. Data assimilation is to seek to find the optimum combination of a numerical model and observation by training numerical model parameters using observed data. Thereby, it would be possible to estimate the state of a system more accurately.

In this study, we apply data assimilation to the integrated transport simulation (TASK3D) of LHD plasma. We use TASK3D code [1] as the numerical simulation model and estimate electron and ion temperatures, $T_\mathrm{e},\ T_\mathrm{i}$. We assume the following turbulent heat transport models[2, 3]. Their coefficients, $C_\mathrm{e},\ C_\mathrm{i}$ are also estimated.

$$\text{Electron (gyroBom model)}: \quad \chi_\mathrm{e}^\mathrm{TB} = C_\mathrm{e}\left(\frac{T_\mathrm{e}}{eB}\right)\left(\frac{\rho_\mathrm{e}}{a}\right)$$

$$\text{Ion (gyroBom+gradT model)}: \quad \chi_\mathrm{i}^\mathrm{TB} = C_\mathrm{i}\left(\frac{T_\mathrm{i}}{eB}\right)\left(\frac{\rho_\mathrm{i}}{a}\right)\left(\frac{aT_\mathrm{i}'}{T_\mathrm{i}}\right)$$

Here, B is the magnetic field strength, ρ is the larmor radius, and a is the plasma minor radius. Time series of observed data $T_\mathrm{e}(t)$ and $T_\mathrm{i}(t)$ are assimilated by the Ensemble Kalman Filter (EnKF)[4], which is one of the data assimilation methods. We use the experment data of NBI heated plasma in LHD (shot: 114053) as the time series observed data.

2 Simulation models

In data assimilation, optimizing numerical models with observations is allowed by replacing the constants, variables and initial values of the models with probability distributions (state vector). Observations are also replaced with probability distribution (observation noise). Data assimilation is the loop of the two steps: prediction and filter. In prediction step, time evolution of the probability distributions is calculated based on the numerical models. The distributions of prediction are expanded by system noise, which occurs with time evolution using the numerical models. In filter step, the prediction is compared to the observation data and the state vector is optimized. The probability distributions become sharp in filter step. For this cause also, it is necessary to expand the distributions by system noise. The variance-covariance matrixes of system noise and observation noise are hyperparameters of data assimilation. Although there are several methods of data assimilation, we use the EnKF, which can be applied for more general numerical models.

The EnKF is Monte Carlo approximation of the Kalman Filter (KF) [4]. In the KF, linear systems are considered in time evolution, and all probability density functions are assumed to be Gaussian. The EnKF is an extended KF so that nonlinear system models can be used by representing probability density functions by ensemble. Time evolution of the probability density functions is calculated by developing each ensemble member with the numerical simulation models.

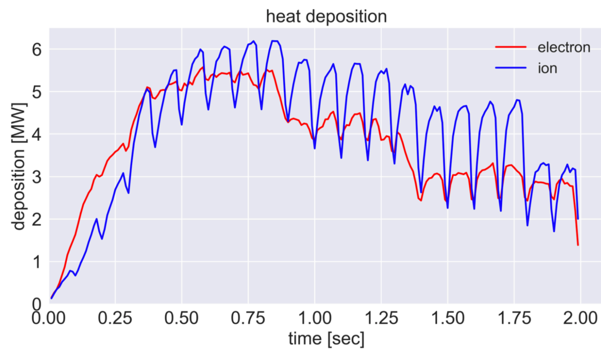

Figure 1: NBI heat deposition evaluated by GNET-TD code.

In this study, we fix the variance-covariance matrix of observation noise, and determine the matrix of system noise using a maximum likelihood estimation. Likelihood is the probability that the observation data is obtained actually from estimated probability distribution. Maximum likelihood estimation is to seek the parameter θ that gives the maximum likelihood. The log likelihood formula for data $n = 1 \sim N$ is

$$l(\theta) = \sum_{n=1}^{N} \log p(\mathbf{y}_n | Y_{n-1}) \simeq \sum_{n=1}^{N} \log \left(\sum_{j=1}^{m} \alpha_n^{(j)} \right) - N \log m,$$

where, for each ensemble member j,

$$\alpha_n^{(j)} = \frac{1}{\sqrt{(2\pi)^l |R_n|}} \exp \left\{ \frac{1}{2} (\mathbf{y}_n - H\mathbf{x}_{n|n-1}^{(j)})^{\mathrm{T}} R_n^{-1} (\mathbf{y}_n - H\mathbf{x}_{n|n-1}^{(j)}) \right\},$$

$\mathbf{y}$ is the observation data vector (dimension l), $\mathbf{x}$ is the state vector, R is the variance-covariance matrix of observation noise, and H is the observation matrix [4].

We simulate NBI heated plasma of LHD (shot 114053). The heat deposition is evaluated by GNET-TD code [5] as in figure1. We set the cycle of data assimilation to 40 ms and the number of ensemble members to 100. The standard deviation of observation noise is fixed to 0.2 keV and we assume that the system noise for T_{e} is 1.2 times that for T_{i}, because the discrepancy between the observations and the estimated values by TASK3D in T_{e} is greater than that in T_{i}.

3 Simulation results

The result of the maximum likelihood estimation for the system noise are shown in figure 2. From this results, it is assumed that the proper noise variance for T_{e} is 1.2 keV^2 ($\sim$1.1 keV) and that for C_{e} and C_{i} are 4.5 and 1.5. The variance for T_{e} which is larger than 1.5 keV^2 ($\sim$1.2 keV) is not proper, because the noise is so strong that the probability distributions diverge.

The results of the prediction for T_{e} using data assimilation with the proper system noise are shown in figure 3. Improvement of the accuracy about T_{e} estimates can not be seen before 1.0 sec, and the estimates take profiles close to the estimates by only TASK3D. This is because the profiles of T_{e} are predicted more strongly based on the factors other than the variables in the state vector.

The results of the prediction for T_{i} using data assimilation are shown in figure 4. In this case, improvement of the accuracy about T_{i} estimates can be seen. Figure 5 is the results of C_{e} and C_{i}

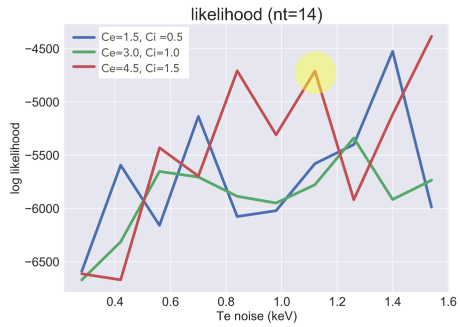

Figure 2: Log likelihood for various system noise variance ($N = 14$).

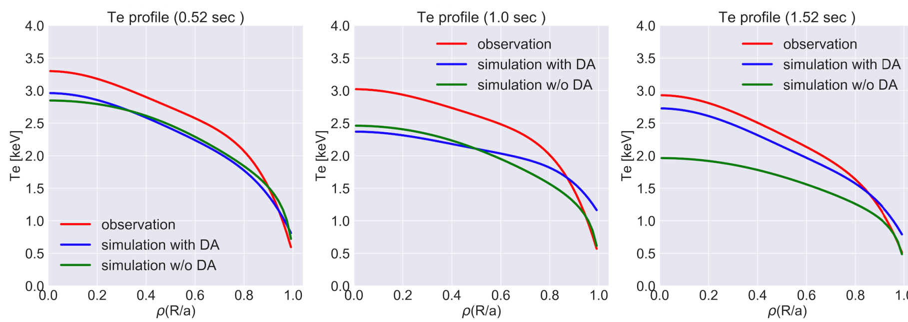

Figure 3: T_{e} profiles of the observations, the estimates using data assimilation and the estimates by only TASK3D.

estimates averaged in radial direction. There are quite differences between the estimates and the conventional fixed values [5].

4 Summary

We have introduced data assimilation method to integrated transport simulation (TASK3D) of LHD plasma. The strength of the system noise have been determined by maximum likelihood method. We have seen improvement of the accuracy about T_{i} estimates, on the other hand, have not seen that about T_{e} estimates.

In future, we will include the particle density and the NBI head deposition into the state

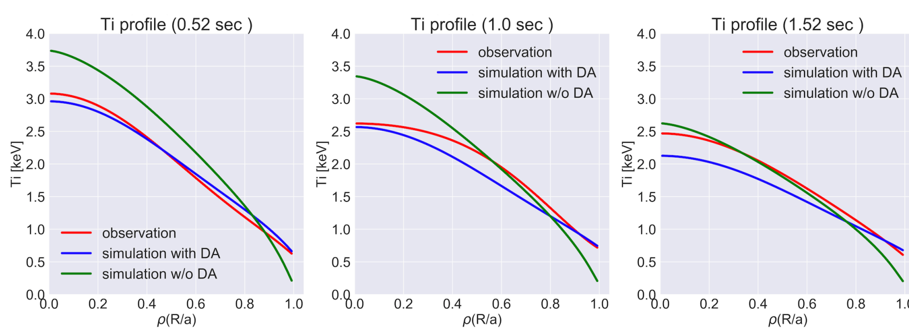

Figure 4: T_{i} profiles of the observations, the estimates using data assimilation and the estimates by only TASK3D.

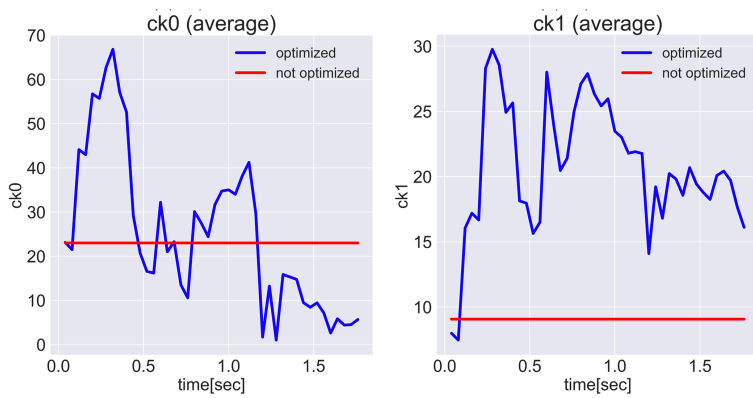

Figure 5: C_e(left) and C_i(right) profiles optimized using data assimilation.

vector, and adjust strength of system noise and observation noise more finely.

References

[1] S. Murakami, et al., Plasma Phys. Control. Fusion **57**, 054009 (2015).

[2] A. Wakasa et al., THC/P4-29, 23rd IAEA Fusion Energy Conf., Daejeon, Korea, (2010).

[3] A. Wakasa et al., Proc. 39th EPS Conf. and 16th Int. Congress on Plasma Physics (2012) P2.028

[4] T. Higuchi, et al., Data douka nyumon [Introduction to data assimilation]. Tokyo: Asakura syoten, (2017).

[5] H. Yamaguchi, et al., JPS Conf. Proc. **1**, 015045 (2014).

Chirality of helical flows in plasma turbulence

M. Sasaki[1,2,*], N. Kasuya[1,2], K. Itoh[2,3], S. Toda[4], T. Yamada[2,5], Y. Kosuga[1,2], Y. Nagashima[1,2], T. Kobayashi[4], H. Arakawa[6], K. Yamasaki[1], A. Fujisawa[1,2], S. Inagaki[1,2], and S.-I. Itoh[1,2]

[1]Research Institute for Applied Mechanics, Kyushu University, 816-8580, Japan
[2]Research Center for Plasma Turbulence, Kyushu University, 816-8580, Japan
[3]Institute of Science and Technology Research, Chubu University, 487-8501, Japan
[4]National Institute for Fusion Science, 509-5292, Japan
[5]Faculty of Arts and Science, Kyushu University, 819-0395, Japan
[6]Shimane University, Graduate School of Engineering, 690?8504, Japan

1 Introduction

Helical flows are ubiquitous in nature. In magnetized confined plasmas, helical flows that consists of flows in the parallel and perpendicular to the magnetic field directions are driven spontaneously. The parallel flow is related to toroidal intrinsic rotations [1] and is sometimes driven by externally injected momentum. The perpendicular flow is related to zonal flows and poloidal mean flows [2]. These flows contribute to the stabilization of the MHD instabilities and the suppression of the transport. Flow bifurcations have often been observed; the inversions of the toroidal flow [1], the poloidal flow [3]. The topology of the helical flow is bifurcated in these cases, where the topology is sometimes characterized by the chilarity. In such a plasma, multiple free energy sources for instabilities coexist. The temperature and density gradients drive the drift wave type instabilities. The inhomogeneities of flows excite Kelvin-Helmholtz instability, the interchange mode, and the D'Angelo mode. The fundamental processes of the formation of the helical flow in such a system should be understood.

2 Model

We perform a three-dimensional simulation of turbulence in magnetized cylindrical plasmas [4]. The density and the parallel flow are assumed to have their gradients in radial direction. In order to account for a situation when the density and the parallel flow are inhomogeneous in space, the particle and parallel momentum sources are introduced. The intensities of the sources control the stabilities of the resistive drift wave and the D'Angelo mode. In order to change the dominant instability, the simulations are performed by changing the density source intensity shot-by-shot with the fixed parallel momentum source.

3 Results

By the change of the particle source intensity, the bifurcation of the turbulent states is found. The transitions among three states are observed: the D'Angelo / resistive drift wave are domi-

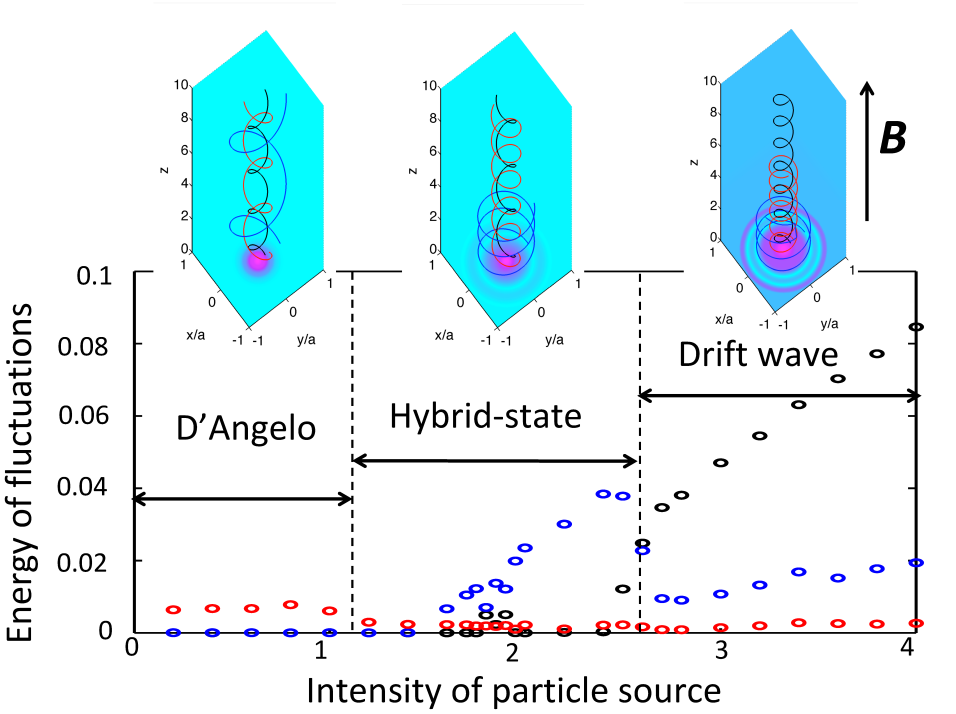

Fig. 1: Energy of each fluctuation as a function of the intensity of the particle source. The stream lines of the mean helical flows are shown for three different cases.

nant when the particle source intensity is small / large, respectively. In the intermediate region, the hybrid mode becomes dominant, which has a characteristics both of the D'Angelo mode and the drift wave, but is a different type of mode [5]. The hybrid mode is driven by both the density gradient and the parallel flow shear. The flow topology is also bifurcated, associated with the transition of the turbulent states. The turbulent fluctuations drive the mean azimuthal flows and induce the parallel momentum flux, so that the flow with the structure of co-axial helix is formed. The each fluctuation energy and the associated helical flows are shown in Fig.1. Depending on the turbulent states, the spatial patterns of the fluctuation change, which leads to the change of spatial structures of the momentum transport, and the flow formation. The results illustrate the generic feature of turbulence flow generation in non-equilibrium magnetized plasmas.

References

[1] P. H. Diamond, et. al., Nucl. Fusion, 53, 104019 (2013).
[2] P. H. Diamond, et. al., Plasma Phys. Control. Fusion, 47, R35 (2005).
[3] S. Inagaki, et. al., Sci. Rep., 6, 22189 (2016).
[4] M. Sasaki, et. al., Phys. Plasmas, 24, 112103 (2017).
[5] M. Sasaki, et. al., Plasma Fusion Res. 12, 1401042 (2017).

基礎実験装置のプラズマ不安定性に関するシミュレーション研究

Study of plasma instability by numerical simulations in basic experimental devices

N. Kasuya, T. Ohno [1], M. Sasaki and M. Yagi [2]
Research Institute for Applied Mechanics, Kyushu University, Kasuga, Fukuoka 816-8580, Japan
[1] Interdisciplinary Graduate School of Engineering Sciences, Kyushu University, Kasuga, Fukuoka 816-8580, Japan
[2] National Institute for Quantum and Radiological Science and Technology, Obuchi, Rokkasho, Aomori 039-3212, Japan
E-mail: kasuya@riam.kyushu-u.ac.jp

Clarifying fundamental mechanisms of turbulence is important in magnetic confined fusion plasmas [1], and researches on structural formation of plasma turbulence has been progressing by using linear devices [2]. A linear device has a cylindrical shape without magnetic curvature and can produce high density plasmas, so is suitable for basic experiments to observe plasma instabilities in details [3]. Numerical simulations of linear devices have been also carried out, and a reduced fluid model for drift wave turbulence is used to describe the 3-D turbulence [4]. For understanding structural formation mechanism, identification of the spatial structure of eigenmodes as the drive of turbulence. In basic experimental devices, the typical spatial scales of the device and gyro-motion of ions are close to each other, so the finite Larmor radius (FLR) effect is not negligible. A mode with the wave length comparable to the effective ion Larmor radius can become unstable even in low ion temperature plasmas [5]. Here we develop a global simulation code for the ion-temperature-gradient (ITG) instability in linear devices [6]. For the first step, linear characteristic of the ITG instability [7] is investigated using the parameter set of PANTA linear device [8]. The parameter dependency is evaluated with a gyro-fluid model to identify influence of the FLR effect.

Fluid models are convenient for analyzing global mode structures in collisional plasmas. The following set of linearized gyro-fluid equations [9] is used, where the magnetic curvature terms can be eliminated for the analysis of the cylindrical configuration;

$$\frac{dn}{dt} + \nabla_{//} u_{//} + \left(1 + \eta_{\perp} \frac{\hat{\nabla}_{\perp}^2}{2}\right) \frac{1}{L_n} \frac{\partial \Psi}{\partial y} = 0\,, \tag{1}$$

$$\frac{du_{//}}{dt} + \nabla_{//}\left(\tau n + T_{//} + \Psi\right) = 0\,, \tag{2}$$

$$\frac{1}{\tau}\frac{dT_{//}}{dt} + \nabla_{//}\left(2u_{//} + \frac{q_{//}}{\tau}\right) + \eta_{//}\frac{1}{L_n}\frac{\partial \Psi}{\partial y} = -\frac{2\nu_{ii}}{3\tau}\left(T_{//} - T_{\perp}\right), \tag{3}$$

$$\frac{1}{\tau}\frac{dT_{\perp}}{dt} + \nabla_{//}\frac{q_{\perp}}{\tau} + \left[\frac{\hat{\nabla}_{\perp}^2}{2} + \eta_{\perp}\left(1 + \hat{\hat{\nabla}}^2\right)\right]\frac{1}{L_n}\frac{\partial \Psi}{\partial y} = \frac{\nu_{ii}}{3\tau}\left(T_{//} - T_{\perp}\right), \tag{4}$$

where n is the ion density, $u_{//}$ is the ion velocity, T is the ion temperature, τ is the ratio between ion and electron temperature at the plasma center, η is the ratio between the density and temperature gradient length, and the subscripts // and $\perp$ represent the quantities in the parallel and perpendicular directions to the magnetic field, respectively. The other definitions of the parameters are described in Ref. [6]. The gyro-averaged potential Ψ is represented as $\Psi \equiv$

$\Gamma_0^{1/2}\Phi$ with operators $\Gamma_0^{1/2} = (1+b\tau/2)^{-1}$ and $b = -\nabla_\perp^{\,2}$. Operator b gives the square of the perpendicular wavenumber $k_\perp^2$, which corresponds to the magnitude of the FLR effect. Two modified Laplacian operators $\hat{\nabla}_\perp^2$ and $\hat{\hat{\nabla}}^2$ are introduced to include the FLR effects. The quasi -neutrality relation is given to be

$$\Gamma_0\left(n - \frac{b/2}{1+b\tau/2}T_\perp\right) - (1-\Gamma_0)\frac{\Psi}{\tau} = \Psi \qquad (5)$$

to determine the relation between the density and potential. The Fourier-Bessel expansion is used to calculate the eigenmode structures. The global analysis using this set of equations considers the boundary condition to determines the radial mode structure, which gives the values of the perpendicular wavenumber [6]. Figure 1(a) shows the dependency of the growth rate on τ and η. The ITG instability is unstable when the ratio of the ion temperature gradient to the density gradient η exceeds the threshold value η_c. The local analysis, as in Fig. 1(b), confirms to reproduce the global analysis result by adjusting the wavenumber to that obtained from the global analysis. The local model with linearization $d/dt \to -i\omega$, $\nabla_{//} \to ik_z$, $\partial/\partial y \to ik_\theta$ gives the following dispersion relation;

$$\begin{aligned}&\omega^3 - \frac{2\tau}{3}\left[-A_2F + \left(\frac{3}{2\tau} - F\right)(1+\eta b_1)\right]\frac{\omega_*}{A_1}\omega^2 \\ &\quad -\frac{2\tau}{3}k_Z^{\,2}\left[\frac{5}{2} + \frac{1}{A_1}\left(\frac{3}{2\tau} - F\right)\right]\omega - \frac{2\tau}{3}k_Z^{\,2}(1+F\tau)A_2\frac{\omega_*}{A_1} = 0\end{aligned}\ , \qquad (6)$$

where

$$A_1 = \left(b + \frac{b^2\tau}{4}\right)(\tau+1)+1 \ , \quad A_2 = -1 + b_1 + \left(\frac{3}{2} - b_1 + b_2\right)\eta \ , \quad F = \frac{b/2}{1+b\tau/2} \ , \quad b_1 = -\tau F \ ,$$

$$b_2 = -2\tau F + \frac{b^2\tau^2/2}{(1+b\tau/2)^2}\text{, and }\ \omega_* = \frac{k_\theta}{L_n}. \qquad (7)$$

With the parameters of the linear device the condition for the unstable ITG mode can be reduced to

$$A_2 > 0. \qquad (8)$$

For small τ, η_c is given as

$$\eta_c = \frac{2}{3} + \frac{5}{9}b\tau. \qquad (9)$$

The critical value η_c changes depending on the magnitude of τ. This dependency is related to the FLR effect. Without the FLR effect, $b = 0$, no dependency on τ appears as in Fig. 1(c). In the case of the resistive drift wave instability, break of the Boltzmann relation $n \neq \Psi$ is important for the destabilization. In this model, the FLR effect can break the Boltzmann relation, as Eq. (5), which affects the instability, but is not strong enough, so this effect alone cannot make the mode unstable.

In this way, numerical analyses using a gyro-fluid model have been performed to investigate the FLR effect on ITG instability in cylindrical plasmas. A spectrum code with Fourier-Bessel expansion has been developed for the analysis of global mode structures. The analytical expression of η_c is obtained from the local dispersion relation. Its τ dependency comes from the FLR effect. Torus devices are used for fusion researches, and for investigation of global structures and their dynamics in torus, PLATO project is now progressing to establish a plasma turbulence observatory [10]. Construction of the platform for analyzing 3-D dynamics of plasma instabilities with a variety of simulation codes is necessary for comparison between experiments and simulations.

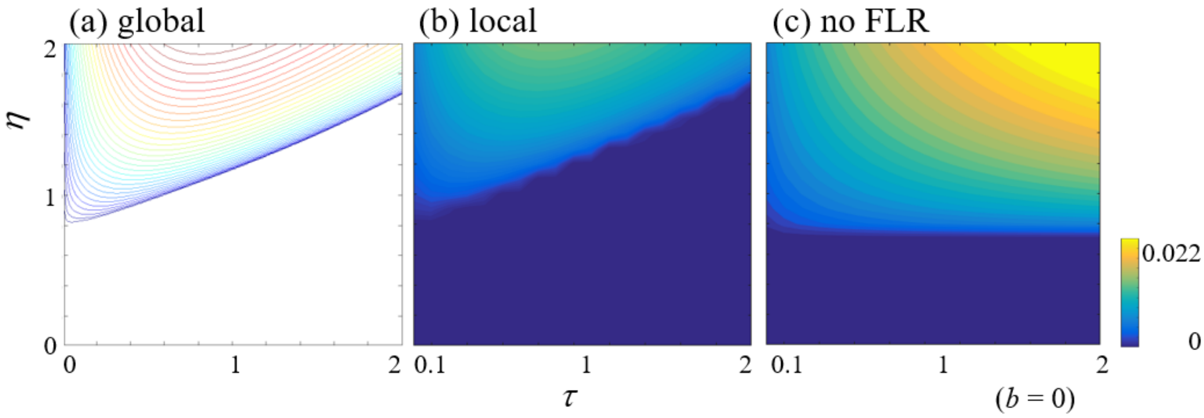

Fig. 1: Dependencies of the growth rate of the ITG instability on τ and η. The mode with azimuthal mode number 2 and axial mode number 1 is calculated with the experimental parameters in the PANTA device. The dependencies from (a) the global model and the local model (b) with and (c) without the FLR effect are shown.

Acknowledgements

This work was partly supported by JSPS KAKENHI Grant Number (JP16K06938, 17H06089), by the collaboration program of NIFS (NIFS17KNST112, NIFS18KNXN373) and RIAM of Kyushu University.

References

[1] P. H. Diamond, et al., Plasma Phys. Control. Fusion **47**, R35 (2005).
[2] G. R. Tynan, et al., Plasma Phys. Control. Fusion **51**, 113001 (2009).
[3] S. Inagaki, et al., Sci. Reps. **6**, 22189 (2016).
[4] N. Kasuya, M. Yagi, K. Itoh and S.-I. Itoh, Phys. Plasmas **15**, 052302 (2008).
[5] Y. Miwa, et al., Plasma Fusion Res. **8**, 2403133 (2013).
[6] T. Ohno, et al., Plasma Fusion Res. **13**, 1401081 (2018).
[7] A.K. Sen, et al., Phys. Rev. Lett. **66**, 429 (1991).
[8] G. Hattori, et al., Plasma Fusion Res. **10**, 3401060 (2015).
[9] W. Dorland and W. Hammet, Phys. Fluids B **5**, 812 (1993).
[10] A. Fujisawa, AIP Conf. Proc. **1993**, 020011 (2018).